August 2007

Femtosecond Laser Microprocessing of Aluminum Films and Quartz

David Doerr

University of Nebraska - Lincoln, doerr@excimer.unl.edu

Follow this and additional works at: http://digitalcommons.unl.edu/elecengtheses

Part of the Electrical and Computer Engineering Commons

Doerr, David, "Femtosecond Laser Microprocessing of Aluminum Films and Quartz" (2007). *Theses, Dissertations, and Student Research from Electrical & Computer Engineering*. 2.
http://digitalcommons.unl.edu/elecengtheses/2

This Article is brought to you for free and open access by the Electrical & Computer Engineering, Department of at DigitalCommons@University of Nebraska - Lincoln. It has been accepted for inclusion in Theses, Dissertations, and Student Research from Electrical & Computer Engineering by an authorized administrator of DigitalCommons@University of Nebraska - Lincoln.

Femtosecond Laser Microprocessing of Aluminum Films and Quartz

by

David W. Doerr

A DISSERTATION

Presented to the Faculty of

The Graduate College at the University of Nebraska

In Partial Fulfillment of Requirements

For the Degree of Doctor of Philosophy

Major: Interdepartmental Area of Engineering

(Electrical Engineering)

Under the Supervision of Professor Dennis R. Alexander

Lincoln, Nebraska

August, 2007

Femtosecond Laser Microprocessing of Aluminum Films and Quartz

David W. Doerr, Ph.D.

University of Nebraska, 2007

Advisor: Dennis R. Alexander

Laser micro and nano-machining using sub-picosecond laser pulses has become a very active area of research, driven by the development of more user-friendly lasers. An improved understanding of the advantages and limitations of using these lasers when processing various materials is desirable.

Ablation of 20 nm thick aluminum films was carried out using pulse widths from 300 fs to 6 ns to achieve sub-micron ablation diameters. Resolution and quality of the resulting craters is compared and discussed. The minimum crater diameter obtained with complete ablation of the film was 130–260 nm for a 400 nm wavelength, 400 fs pulse focused with a microscope objective with numerical aperture of 0.85. A large window of pulse energies exists where clean ablation of 20 nm Al films can be obtained with minimal damage to the substrate for pulses shorter than 4 ps. This pulse energy range was a factor of 2.6-7.3 times the ablation threshold for pulses less than 4 ps and decreased with increasing laser pulse width to ≤ 1.2 for 6 ns pulses. Nanoscale protusions (nanobumps and nanospikes) with heights from 20-140 nm were created at fluences just below the ablation threshold. The laser damage threshold of the film is also measured and compared to a theoretical model.

The quality of fs-laser micromachined quartz crystals was also examined. Fluence was varied and the entrance and exit side examined for microcracking to determine optimal processing parameters. Cuts with a high quality laser entrance side without

microcracking could be obtained for fluence ranges from 2.5-13 J/cm^2 while micro-cracking at the cut entrance is observed at 16 J/cm^2. Damage on the exit side of the sample was observed within a distance of 50 μm from the center of the cut and runs parallel to the laser cut.

ACKNOWLEDGEMENTS

I would like to thank several people for their assistance and support in the process of my dissertation work. Thanks go out to my advisor, Dennis Alexander, for his support and for establishing and maintaining the high quality facilities and equipment used in this research. I would also like to thank my other committee members, Ned Ianno, Paul Snyder and Tom Marley for their willingness to be on my committee. Thanks also to some former grad students, Mark Woehrer and Brian Mihulka for development and modification of the motion control software which was used in this work. Thanks to John Schiffern and others in the lab for being there for interesting discussions. Lastly, I would like to thank my family for their support and encouragement.

TABLE OF CONTENTS

LIST OF FIGURES

LIST OF TABLES

NOMENCLATURE

Chapter 1

Introduction and Literature Review

Laser ablation is an important process in a wide range of applications including micromachining of materials, thin film production and nanoparticle production. An understanding of the laser-material interaction process is important in these applications in order to produce the desired results. "Clean" ablation with minimal debris and thermal damage such as melting and cracking to the surrounding area is desired in laser micromachining applications. A more complete understanding of how laser parameters such as pulse duration, wavelength, polarization, fluence, etc., as well as other parameters such as the ambient pressure, etc., affect the results is desired. Solid-state femtosecond lasers such as the self-mode-locked Ti:sapphire have just recently become commercially available and a great amount of research is ongoing to understand the basic laser-material interaction process with these shorter pulsed lasers and determine what advantages they may have compared to more traditional lasers with pulse widths of nanoseconds and longer in materials processing applications.

This chapter will give a brief review of the literature and the effects of various parameters affecting the laser-material interaction process. A review of studies of picosecond and shorter time-scale laser-material interaction for various materials above the laser damage threshold are also presented. Finally, research objectives and the outline of this dissertation are discussed.

1.1 Materials Processing Using Ultrashort Pulse Lasers

The study of the laser-material interaction using short pulse lasers is an active area of research. Research into the details of topics such as the transfer of energy from free carriers to the lattice, the mechanism of free carrier generation in dielectrics and the ablation mechanisms for various materials are ongoing. Investigations of the quality of the ablated area (surface roughness, chemical composition, surrounding damage, etc.) for various materials have also been undertaken. This section will provide an overview of the studies of ultrafast ablation and micromachining that have focused on metals and quartz as targets.

1.1.1 Ultrashort Pulse Laser Interaction with Metals

The laser ablation process for metals with femtosecond pulses consists of several steps beginning with transfer of energy from photons to free electrons, diffusion and thermalization of these electrons, and a transfer of the energy to the lattice through scattering. For metals the characteristic time for the transfer of energy from the electrons to the lattice is a few picoseconds. Thus for pulses shorter than a few picoseconds a nonequilibrium situation exists between the electron and lattice system. The ablation mechanism for sub-picosecond laser pulse interaction with metals has been described as thermal, with the actual transfer of energy from the lattice and ablation occuring after the laser pulse.[1,2]

Studies of the damage threshold of metals vs. laser pulse width have demonstrated that the ablation threshold is controlled by thermal diffusion for longer pulses (> 10–100's ps) and is controlled by the absorption coefficient of the material and diffusion of hot electrons for shorter pulses.[1,3,4] For pulses shorter than a critical pulse width the heated depth when electrons and lattice reach equilibrium is expected to be relatively

constant and determined by diffusion of nonequilibrium electrons. There is then a critical pulseswidth, τ_c, where the damage threshold is not changing significantly for pulses which are shorter than this parameter and critical heated depth, L_c, for pulses shorter than τ_c.[5] The critical heated depth is dependent upon the electron-phonon coupling factor. This parameter describes how rapidly energy is transferred from the initially laser-heated electron to the lattice and is characteristic of each metal.

The expansion of material during the laser pulse is a fraction of a wavelength of light for subpicosecond pulses at fluences just above the ablation threshold and is negligible for pulses less than 100 fs due to the extremely short time scales involved.[6,7] This is in contrast to laser-material interactions with longer pulses which have been described as "plasma-mediated". On these longer time scales the initial part of the laser pulse causes heating and material expansion and the remainder of the laser pulse continues to heat the ejected material, and the resulting plasma may even shield the target surface from the laser radiation. Thus, for subpicosecond pulses, a near-solid-density plasma can be produced with pulses of sufficient intensity.

The lateral resolution of the ablation pit can be controlled by adjusting fluence and can be used to obtain submicron ablation diameters. Fig. 1.1 shows this concept. By adjusting the peak fluence at the center of the gaussian beam so that it is just above the ablation threshold, an ablation crater diameter much less than the characteristic diameter, d_0, of the laser beam can be achieved. The ablation or damage diameter can be expressed as:

$$d(F) = \frac{d_0}{\sqrt{2}}\sqrt{\ln(F/F_{th})}$$

where F is the peak fluence, $d(F)$ is the ablation/damage diameter, d_0 is the $1/e^2$ beam diameter of the gaussian beam and F_{th} is the ablation/damage threshold
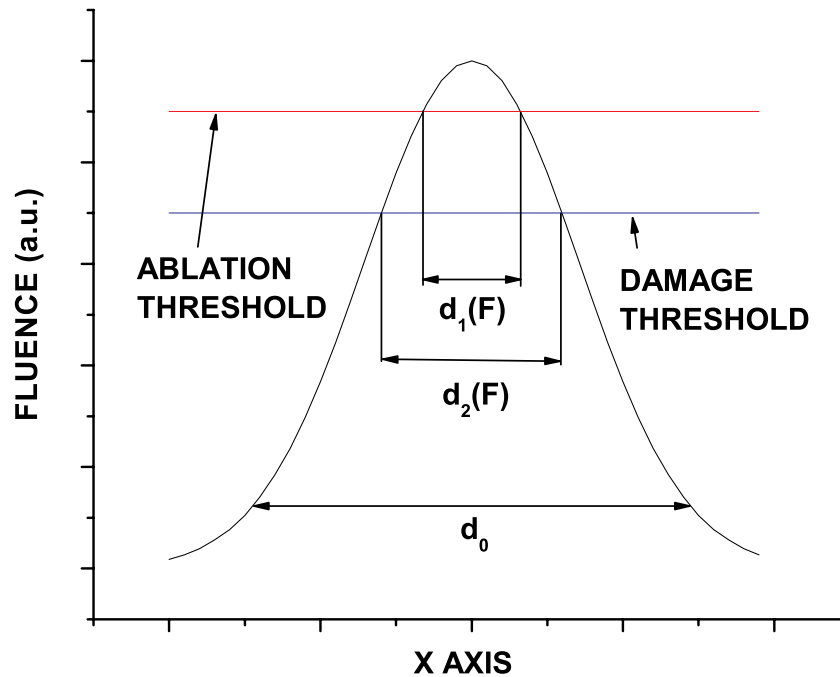
Figure 1.1: Concept of fluence dependent ablation diameter. The fluence at the center of the gaussian beam is adjusted to be just above the ablation threshold, creating an ablation crater of diameter $d_1(F)$ and damage diameter $d_2(F)$.

fluence. Using this technique, ablated features as small as 30 nm have been produced in glass.[8]

By adjusting the peak fluence above the damage threshold but below the ablation threshold, raised structures have been created from gold films by illumination with single shot fs pulses. Fig. 1.2 shows a diagram of nanobump and nanojet features which have been observed after single shot 30 fs laser excitation of gold at fluences just above the damage threshold.[9] Research on the physical mechanisms of nanobump/nanojet formation is also an active area. Smooth nanobumps have been observed at lower fluences without a nanojet feature, and have been modeled as plastic deformation of the film which occurs without melting.[10] As fluence is increased, the central area of the film (with the highest temperature for a gaussian spatial laser

energy distribution) undergoes melting. From volumetric considerations, the gold nanobumps and nanojets must be hollow structures. A hollow nanojet may form when the molten material continues to travel while the unmolten film is slowing. The flowing molten material cools into the nanojet for low enough fluences or becomes ejected at higher fluences.
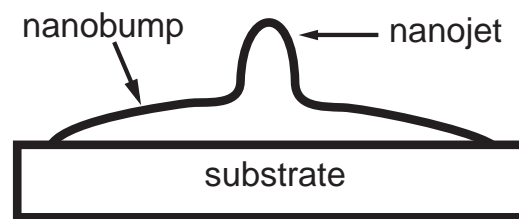
Figure 1.2: Diagram of nanobump and nanojet created by single pulse fs laser irradiation of Au film just above the damage threshold.

1.1.2 Ultrashort Pulse Laser Interaction with Quartz

Fig. 1.3 shows the electronic structure of quartz and the absorption processes possible when interacting with high intensity 800 nm (1.55 eV) light. Traditionally, multi-photon ionization (MPI) is believed to be the primary electron-hole pair (e-h pair) generation mechanism for intrinsic quartz. These free electrons can then be accelerated to high energies, and if they reach the bandgap energy, 9.2 eV, impact ionization can create more free carriers in an avalanche mechanism. Several studies have attempted to sort out the importance of these two carrier generation mechanisms for various materials.[11–14] Transfer of energy from the electrons to the lattice will occur through scattering and is called free carrier absorption (FCA). A newer model for laser damage finds that MPI does not play a dominant role but instead Zener ionization dominates and is followed by a combination of Zener and Zener-seeded avalanche ionization.[8]
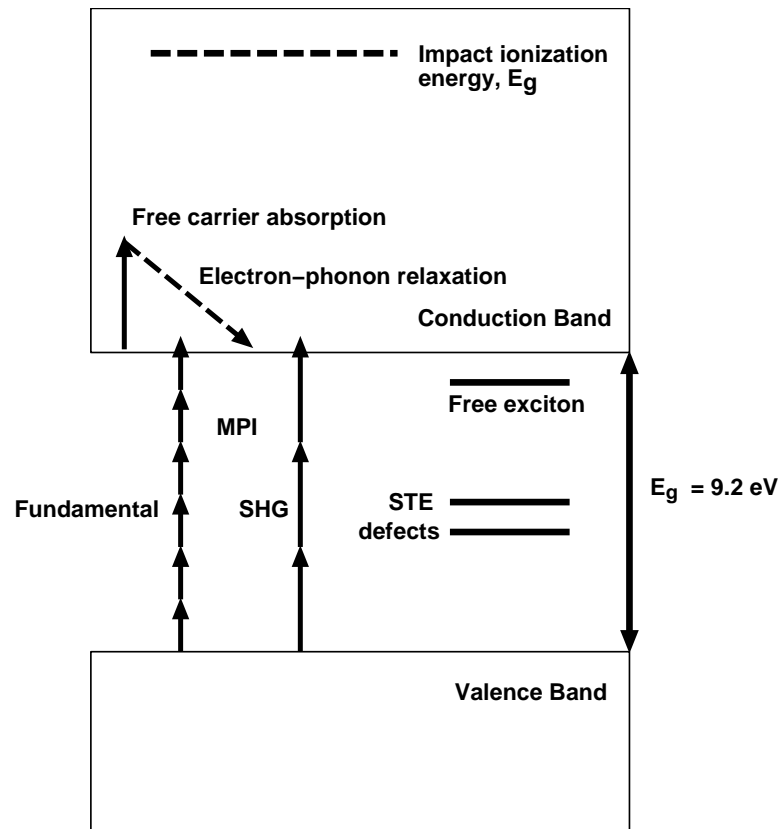
Figure 1.3: Energy band diagram and absorption processes in quartz. 800 nm light (1.55 eV) (Fundamental) is assumed. Second harmonic generation (SHG) and higher order processes may become effective, particularly for bulk absorption. Free carrier generation begins with multi-photon ionization (MPI) for intrinsic material. Free carrier excitation followed by electron-phonon relaxation transfers heat to the lattice. Impact ionization may become another source of free carrier generation for high energy electrons. Free excitons, self-trapped excitons (STE's) and defects produce additional levels in the bandgap.

Nonlinear processes such as second harmonic generation (SHG) and supercontinuum generation processes may also play a role in the ablation mechanism and are shown on the diagram. Supercontinuum generation results in a broad emission spectrum centered about the laser wavelength.[15] The shorter wavelengths of light which are generated may be absorbed through a more efficient MPI process than the fundamental. Efimov[16–18] has concluded that supercontinuum generation followed by two-photon absorption generates color centers in glasses at fluences below the damage threshold. The laser generated color centers could be removed by annealing. However, permanent color center generation was not observed in fused silica for the absorption spectral range investigated.

Glezer[19] demonstrated that sub-micron dimension "microexplosions" could be formed in fused silica and other materials using 100 fs pulses. These "voxels" (volume pixels) could be formed in a range from threshold energy to three times above it. They appeared to consist of spherical damage regions with an increasing diameter for increasing laser energy in this fluence range. Self-focusing was believed to contribute to the small voxel size. For higher energies, a "head and filament" structure was described with a length of 20-40 microns. No cracking was observed at energies up to 100 times threshold. In contrast, 200 ps and 10 ns pulses produced more cracking and larger damaged areas.

Laser exit side damage was noted in fs laser cutting and drilling of glasses.[20–22] Varel[23] has investigated the drilling of channels through quartz samples. A 75 mm focal length lens was used with 120 fs pulses at 790 nm to obtain 21 micron diameter channels through 1 and 2 mm thick quartz samples. These narrow channels were observed in vacuum but not in atmospheric pressure N_2. More cracking was observed around the entrance hole than the exit hole with relatively little observable damage in the bulk. The peripheral damage around the entrance was also observed to increase

with pulse energy. Picosecond and nanosecond pulses were seen to produce more cracking in the quartz.

1.2   Research Objectives

This dissertation investigates sub-ps laser micromachining of Al films and quartz crystals. Submicron scale ablation of aluminum films is performed using pulse durations from 100's of fs to several ns. The size of ablation diameter and quality of ablation vs. pulse energy of aluminum films is compared. Nanoscale protrusions created just below the ablation threshold for single fs pulses are also presented. The laser damage threshold of the film is also measured and compared to a theoretical model. Femtosecond laser processing of slots in a crystalline quartz sample is also performed. The fluence was varied and the entrance and exit side examined for microcracking to determine optimal processing parameters.

This dissertation is arranged in two self-contained sections, one for laser microprocessing of Al films and the other for fs laser microprocessing of quartz, each in a journal publication format. A summary of conclusions and recommended research and appendixes follow.

REFERENCES

1. S. Preuss, E. Matthias, and M. Stuke, "Sub-picosecond UV-laser ablation of Ni films: Strong fluence reduction and thickness-independent removal," *Appl. Phys. A*, vol. 59, pp. 79–82, 1994.

2. T. Götz and M. Stuke, "Short-pulse UV laser ablation of solid and liquid metals: indium," *Appl. Phys. A*, vol. 64, pp. 539–543, 1997.

3. S. Preuss, A. Demchuk, and M. Stuke, "Sub-picosecond UV ablation of metals," *Appl. Phys. A.*, vol. 61, pp. 33–37, 1995.

4. P. P. Pronko, S. K. Dutta, D. Du, and R. K. Singh, "Thermophysical effects in laser processing of materials with picosecond and femtosecond pulses," *J. Appl. Phys.*, vol. 78, no. 10, pp. 6233–6240, 1995.

5. N. K. Sherman, F. Brunel, P. B. Corkum, and F. A. Hegman, "Transient response of metals to ultrashort pulse excitation," *Opt. Eng.*, vol. 28, pp. 1114–1121, 1989.

6. H. M. Milchberg, R. R. Freeman, S. C. Davey, and R. M. More, "Resistivity of a simple metal from room temperature to 10^6 K," *Phys. Rev. Lett.*, vol. 61, no. 20, pp. 2364–2367, 1988.

7. E. G. Gamaly, "The interaction of ultrashort, powerful laser pulses with a solid target: Ion expansion and acceleration with time-dependent ambipolar field.," *Phys. Fluids B*, vol. 5, no. 3, p. 994, 1993.

8. A. P. Joglekar, H. Liu, E. Meyerhöfer, G. Mourou, and A. Hunt, "Optics at critical intensity: Applications to nanomorphing," *PNAS*, vol. 101, pp. 5856–5861, 2004.

9. J. Koch, F. Korte, T. Bauer, C. Fallnich, A. Ostendorf, and B. N. Chickov, "Nanotexturing of gold films by femtosecond laser-induced melt dynamics," *Appl. Phys. A*, vol. 81, pp. 325–328, 2005.

10. Y. P. Meshcheryakov and N. M. Bulgakova, "Thermoelastic modeling of microbump and nanojet formation on nanosize gold films under femtosecond irradiation," *Appl. Phys. A*, vol. 82, pp. 363–368, 1996.

11. D. Du, X. Liu, and G. Mourou, "Reduction of multi-photon ionization in dielectrics due to collisions," *Appl. Phys. B*, vol. 63, pp. 617–621, 1996.

12. W. Kautek, J. Krüger, M. Lanzner, S. Sartania, C. Spielmann, and F. Krausz, "Laser ablation of dielectrics with pulse durations between 20 fs and 3 ps," *Appl. Phys. Lett.*, vol. 69, pp. 3146–3148, 1996.

13. M. Lenzner, J. Krüger, S. Sartania, Z. Cheng, C. Spielmann, G. Mourou, W. Kautek, and F. Krausz, "Femtosecond optical breakdown in dielectrics," *Phys. Rev. Lett.*, vol. 80, no. 18, pp. 4076–4079, 1998.

14. B. C. Stuart, M. D. Feit, S. Herman, A. M. Rubenchick, B. W. Shore, and M. D. Perry, "Optical ablation by high-power short-pulse lasers," *J. Opt. Soc. Am. B*, vol. 13, no. 2, pp. 459–468, 1996.

15. M. Wittmann and A. Penzkofer, "Spectral superbroadening of femtosecond laser pulses," *Opt. Commun.*, vol. 126, pp. 308–317, 1996.

16. O. M. Efimov, K. Gabel, S. V. Garnov, L. B. Glebov, S. Grantham, M. Richardson, and M. J. Soileau, "Color-center generation in silicate glasses exposed to infrared femtosecond pulses," *J. Opt. Soc. Am. B*, vol. 15, no. 1, pp. 193–199, 1998.

17. O. M. Efimov, K. Gabel, S. V. Garnov, L. B. Glebov, S. Grantham, M. Richardson, and M. J. Soileau, "Photo-induced processes in silicate glasses exposed to IR femtosecond pulses," in *Laser-Induced Damage in Optical Materials: 1996*, vol. 2966 of *Proc. SPIE*, pp. 65–71, 1996.

18. O. M. Efimov, L. B. Glebov, S. V. Garnov, M. J. Soileau, M. Richardson, K. Gabela, and S. Grantham, "Nonlinear coloration and damage of wide gap glasses by femtosecond laser at 0.85 microns," in *Proc. SPIE*, vol. 2796, pp. 245–249, 1996.

19. E. N. Glezer, L. Huang, R. J. Finley, T.-H. Her, J. P. Callan, C. Schaffer, and E. Mazur, "Ultrafast laser-induced microexplosions in transparent materials," in *Laser-Induced Damage in Optical Materials: 1996*, vol. 2966 of *Proc. SPIE*, pp. 392–403, 1996.

20. S. Nolte, M. Will, M. Augustin, P. Triebel, K. Zöllner, and A. Tünnermann in *Lithographic and Micromachining Techniques for Optical Component Fabrication*, vol. 4440 of *Proceedings of SPIE*, (Bellingham, WA), pp. 152–160, SPIE, 2001.

21. N. Kuriyama and Y. Ito, "Third international symposium on laser precision microfabrication," vol. 4830 of *Proceedings of SPIE*, (Bellingham, WA), pp. 567–572, SPIE, 2003.

22. E. Vanagas, J. Kawai, D. Tuzhilin, I. Kudryashov, A. Mizuyama, K. Nakumara, K. Kondo, S. Koshihara, M. Takesada, K. Matsuda, S. Joudkazis, V. Jarutis, S. Matsuo, and H. Misawa, "Glass cutting by femtosecond pulsed irradiation," *J. Microlith., Microfab., Microsyst.*, vol. 3, pp. 358–363, 2004.

23. H. Varel, D. Ashkenasi, A. Rosenfeld, M. Wähmer, and E. E. B. Campbell, "Micromachining of quartz with ultrashort laser pulses," *Appl Phys. A*, vol. 65, pp. 367–373, 1997.

Chapter 2

Aluminum Film Ablation and Nanostructuring

Abstract

Submicron scale ablation of 20 nm aluminum films is performed using pulse durations from 100's of fs to 6 ns. The size of ablation diameter and quality of ablation vs. pulse energy of aluminum films is compared. The minimum crater diameter obtained with complete ablation of the film was 130–260 nm for a 400 fs pulse. A large window of pulse energies exists where clean ablation of 20 nm Al films can be obtained with minimal damage to the substrate for pulses shorter than 4 ps. Nanoscale protrusions which increased with pulse energy up to 150 nm height were created just below the ablation threshold for single fs pulses. The laser damage threshold of the film is also measured and compared to a theoretical model.

2.1   Introduction

Processing materials using ultrashort lasers on a sub-micron scale in a direct-write mode is attractive for many applications. The semiconductor and electronics industries continually require higher resolution methods in manufacturing. Comparison of repairs to lithographic masks using femtosecond and nanosecond laser pulses to remove opaque chrome defects demonstrated better transmission through the substrate after defect removal, less damage to the quartz substrate, and less metal splatter around the repair site when femtosecond pulses were used.[1] One method to enhance spatial resolution takes advantage of the spatially varying intensity of the focused Gaussian laser beam. By adjusting fluence such that only the high intensity peak of the beam is ablating material, resolution less than the laser spot size can be achieved.[2] The success of this method has been noted to be material dependent, particulary when creating structures on the sub-micron scale. Comparison of single pulse, sub-micron ablation of 100 nm chromium and gold films showed a large molten rim surrounding the ablated area for gold while film defects without appearance of melt surrounded the chromium ablation crater.[3] This behavior was believed to be related to the different electron-phonon coupling times between the two materials, affecting the lifetime of the melt.

Different thresholds are also present for different materials, the damage threshold typically being reached when melting of the film occurs and permanently deforms the film and ablation (material removal) occurring at a higher fluence. Irradiation of gold films with single pulses from tightly focused femtosecond lasers produced unique surface protrusions for fluences just above the damage threshold.[3] For 60 nm gold films, a smooth nanoscale bump increases in height with fluence up to hundreds of nm. As fluence is further increased a narrow jet of material grows from the center of

the bump and increases in height up to ~ 1000 nm. As fluence is increased further, the structure becomes unstable and ablation occurs forming a crater in the film. This process is a unique ablation-free way of nanotexturing gold films. Gold has unique properties that are believed to allow this behavior to occur including its plasticity, low melting point and yield stress.[4] Other materials are also expected to exhibit the phenomenon based on their material properties.

This work investigates three main topics. First, the ablation quality achieved with sub-micron laser spots on aluminum film on fused silica using laser pulsewidths from 100's of femtoseconds to 6 nanoseconds is investigated at fluences above the ablation threshold. The scaling of ablation crater diameters with pulse energy, ablation crater rim dimensions and ablated depth vs. pulse energy for different laser pulsewidths are examined. Secondly, raised nanostructures on the aluminum film that were only observed with near-threshold sub-picosecond pulses are investigated. These raised structures were observed at pulse energies between the damage threshold and the ablation threshold. Protrusions with heights of ~ 10–150 nm are observed and the pulse energy range where they are stable and their scaling with pulse energy and repeatability is investigated. The third section compares a damage threshold model appropriate for fs pulses interacting with metal films with experimental data on Al films.

2.2   Experimental

The laser system consists of a regenerative laser amplifier system based on chirped pulse amplification. Low energy seed pulses are provided by a mode-locked Ti:sapphire oscillator (Spectra-Physics, Tsunamai) which is pumped by a diode-pumped cw visible laser (Spectra-Physics, Millennia V). Pulses are amplified in a Ti:sapphire regenerative amplifier system (Photonics Industries, Model TRA-50-2) pumped by an

intracavity frequency doubled, q-switched Nd:YLF laser (Photonics Industries, Model GM-30). By adjusting the compressor in the regenerative amplifier, pulse durations from 150 fs to several ps can be achieved with up to a mJ of energy per pulse. By-passing the compressor after amplication in the regenerative amplifier results in pulse durations of 400 ps. The regenerative amplifier can also produce nanosecond dura-tion pulses by not seeding the amplifier with femtosecond pulses and using cavity dumping. In the work conducted in this project, the femtosecond and 4 ps pulses at 800 nm wavelength are measured with a background-free autocorrelator, while a fast photodiode is used to measure the 400 ps and nanosecond pulses at 400 nm. Pulse to pulse variation of 5–10 percent at 400 nm was typical for all pulse durations. An external synchronization and trigger circuit has been added to the laser system to allow single pulse firing or other slower pulse rate as desired under computer control.

Fig. 2.1 is an overview of the experimental setup. Laser pulses at 800 nm out-put are frequency doubled to 400 nm using a 1 mm thick BBO crystal. For ns pulses, a beam reducer was used before the BBO to increase frequency doubled in-tensities at 400 nm to the values needed for film damage. Dichroic mirrors and a BG-39 filter are used to reject the residual 800 nm light. Neutral density filters and a waveplate/polarizer combination allow variable attenuation of the laser power which was measured with a calibrated photodiode. The beam is focused on the sample using a 60X microscope objective (NA=0.85) for experiments in air and a long working distance objective (NA=0.32) for work in vacuum in the ablation qual-ity/nanostructuring experiments. Film ablation is monitored by imaging the sample surface using backscattered light on a CCD camera using the microscope objective and an imaging lens for ablation quality/nanostructuring experiments. The imaging capability provided a means to find the focal position which minimized the energy required to ablate the film prior to the experiment, ensuring the smallest laser spot at
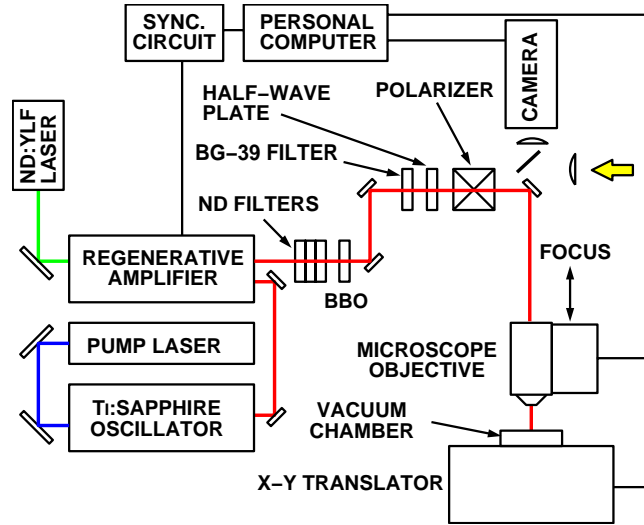
Figure 2.1: Experimental setup.

the sample surface. This camera is also used to monitor the laser beam profile while adjustments are made to the femtosecond laser optical elements to obtain a near-Gaussian beam at the start of the experiment. A 65 mm focal length plano-convex lens was also used for experiments requiring a larger spot-size including film damage threshold measurements.

Computer controlled motion of the sample and focusing lens was performed with Melles Griot Nanomotion translation stages providing XY sample translation and a Z axis for focusing capability. One laser pulse was fired at each site along a path length of 1000 microns at each specified energy level. For experiments in vacuum, a small chamber was attached to the XY translators to provide a 5 mtorr vacuum.

Samples are 20 nm thick aluminum films on fused silica substrates, obtained from CVI Laser Corporation. Aluminum film thickness was estimated to be 20 nm by transmission and reflection measurements at 633 nm using optical constants given in Table 2.1, while AFM examination of the sample after film ablation with fs pulses showed that 30 nm had been removed. A native oxide thickness of 2 to 6 nm or more is

Table 2.1: Physical properties used in model calculations.

Symbol and value	Property	Reference
Aluminum film		
$n = 1.51$, 633 nm; $n = 0.49$, 400 nm	Index of refraction	5
$k = 7.37$, 633 nm; $k = 4.86$, 400 nm	Index of extinction	5
$T_m = 933$ K	Melting point	6
$H_f = 1080$ J/cm^3	Heat of fusion	6
$\rho_f = 2.7$ g/cm^3	Density	7
$K_f = K_0 = 2.2$ J cm^{-1} sec^{-1} K^{-1}	Thermal conductivity	7
$C_f = C_l = 0.9$ J g^{-1} K^{-1}	Lattice heat capacity	7
$D_f = K_f/\rho_f c_f = 0.9$ cm^2/s	Thermal diffusivity	7
$A_e = 9.2$ x 10^{-5} J cm^{-3}K^{-2}	Electronic specific heat coefficient	8
$C_e = A_e T_e$	Electronic specific heat	
$g = 4.9$ x 10^{11}W cm^{-3}K^{-1}	Electron-phonon coupling parameter	8
Fused silica substrate		
$n = 1.47$, 400 nm; $n = 1.46$, 633 nm	Index of refraction	9
1770 K	Softening point	7
$\rho_s = 2.2$ g/cm^3	Density	7
$K_s = 0.014$ J cm^{-1} sec^{-1} K^{-1}	Thermal conductivity	7
$C_s = 0.79$ J g^{-1} K^{-1}	Heat capacity	7
$D_s = K_s/\rho_s c_s = 0.008$ cm^2/s	Thermal diffusivity	7
Aluminum oxide		
$n = 1.79$, 400 nm; $n = 1.77$, 633 nm	Index of refraction	10
$T_m = 2327$ K	Melting point	11
$C_{ox} = 0.78$ J g^{-1} K^{-1}	Heat capacity	11
$\rho_{ox} = 3.97$ g/cm^3	Density	11
$K_{ox} = 0.18$ J cm^{-1} sec^{-1} K^{-1}	Thermal conductivity	11
$D_{ox} = K_{ox}/\rho_{ox} c_{ox} = 0.058$ cm^2/s	Thermal diffusivity	11

typical after exposure to atmosphere and accounts for the difference in thickness estimates by optical means and AFM.[5] The film absorption was measured to be 15 ± 5 % by measuring the reflectivity and transmission of the sample with sub-threshold 300 fs pulses at 400 nm wavelength. Samples ablated in air were ultrasonically cleaned in methanol before contact mode AFM imaging to remove debris and improve the image quality while samples prepared in vacuum were not. Ablated samples were also imaged with an optical microscope.

For ablation quality/nanostructuring experiments, single pulse ablation of the
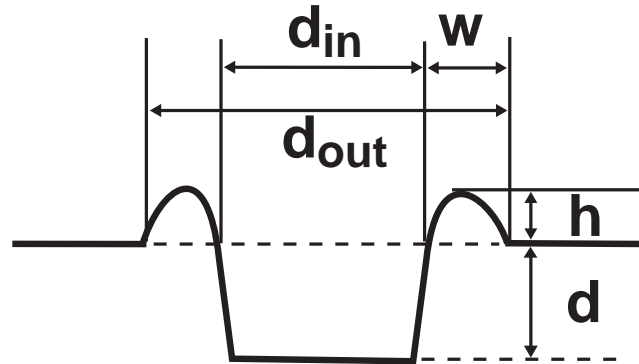
Figure 2.2: Typical ablation crater illustrating the parameters used to characterize the aluminum film damage region.

films was performed in air using pulse durations of 400 fs, 600 fs, 400 ps, and 6 ns, and in a 5 mtorr vacuum with 300 fs, 4 ps and 6 ns duration pulses. Lines were also written by moving 0.2 microns between pulses.

2.3 Results and discussion

2.3.1 Ablation quality

Fig. 2.2 shows a cross-sectional diagram of an ablated hole in the film showing parameters which were measured. Parameters measured as a function of pulse energy include: d_{in}, the crater inner diameter; d_{out}, the crater outer diameter; d, the ablated depth; h, the crater height of molten/deformed material; and the crater rim width, w. The bottom of the crater was not necessarily flat as shown in the diagram. A raised central bump instead of an ablation crater was sometimes observed at fluences just above the damage threshold and no inner diameter measurement was made for this case.

Fig. 2.3 shows the measured ablation depth and crater rim height as a function of pulse energy for different pulse durations. Note the initial pulse energy with negative depths in Fig. 2.3(b), (indicating raised bumps rather than craters) for 300 fs pulses.

Bump formation also occurred for 400 and 600 fs pulses but that data is not shown here. A seperate section will discuss the pulse energy range just above threshold where bump formation occurs for fs pulses.
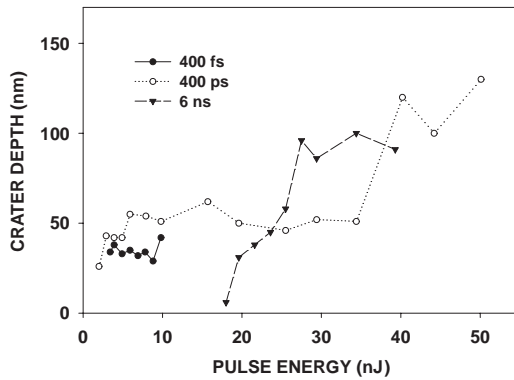
(a) Crater depth in air.
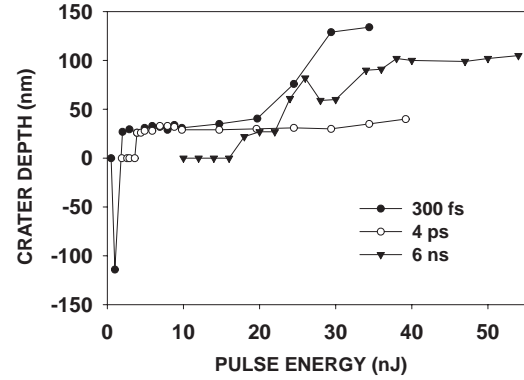
(b) Crater depth in vacuum.
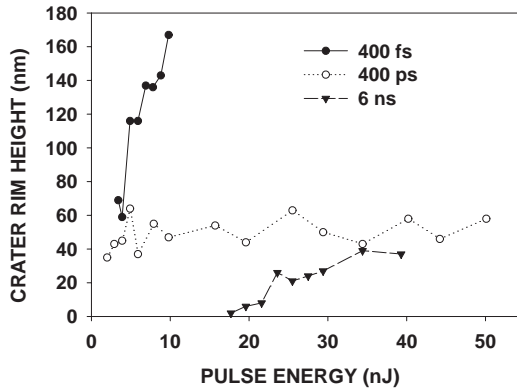
(c) Crater rim height in air.
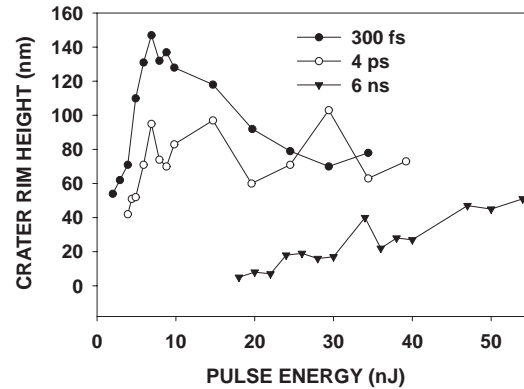
(d) Crater rim height in vacuum.

Figure 2.3: Single-shot crater depth vs. laser pulse energy for 760 torr, (a), and 5 mtorr, (b), for different pulse durations. Negative depths observed for 300 fs pulses near the damage threshold indicate a raised surface of the sample rather than ablation. Crater rim height vs. pulse energy for different pulse durations is plotted for 760 torr, (c), and 5 mtorr, (d). Lines between data points are to help guide the eye.

Comparing the ablation depth vs. pulse energy for different pulse durations, we observe that for pulses of 4 ps and shorter, a broad range of pulse energies gave ablation of only the aluminum film as determined by the nearly constant 30 nm

crater depth as pulse energy increases. In contrast, the 400 ps and 6 ns duration pulses had a much narrower range of pulse energy to remove only the film. We will define the 'clean ablation' range as the range of pulse energies which will completely remove the film but not damage the underlying substrate by creating a melt pit. A crater depth of greater than 35 nm was the criterion for damage to the substrate. Table 2.2 lists the range of 'clean ablation' pulse energies for different pulse durations in air and vacuum. For 4 ps and shorter pulses the energy range for clean ablation was from 2.6–7.3 times the clean ablation threshold while 400 ps and longer pulses had a range of less than 1.5 times the clean ablation threshold.

Table 2.2: Range of pulse energy for ablation with no substrate melting.

Pulse Width	Pressure	Energy range of clean ablation (X times clean ablation threshold)
400 fs	760 torr	2.6
600 fs	760 torr	3.2
400 ps	760 torr	≤ 1.5
6 ns	760 torr	≤ 1.1
300 fs	5 torr	4.9
4 ps	5 torr	7.3
6 ns	5 torr	≤ 1.2

Taller crater rims were created as laser pulses became shorter. In Fig. 2.3 (c) and (d) we note rim heights were from 60–170 nm for the 300 and 400 fs case, dropped to 40–100 nm for the 4 ps case, 40–60 nm for 400 ps pulses and were less than 50 nm for 6 ns pulses. AFM images and cross-sections of ablation craters for the 400 fs pulses are shown in Figs. 2.4 and 2.5. Note the increase in crater rim height as pulse energy increases. Substrate damage appears as a molten pit in the center of the ablation crater at 10 nJ, above the 'clean ablation' threshold. The 2.5 and 3.5 nJ pulse energies are just above ablation threshold and a crater inner diameter of 130 nm was achieved for 2.5 nJ pulses and 260 nm for 3.5 nJ pulses.

(a) 2.5 nJ   (b) 3.5 nJ
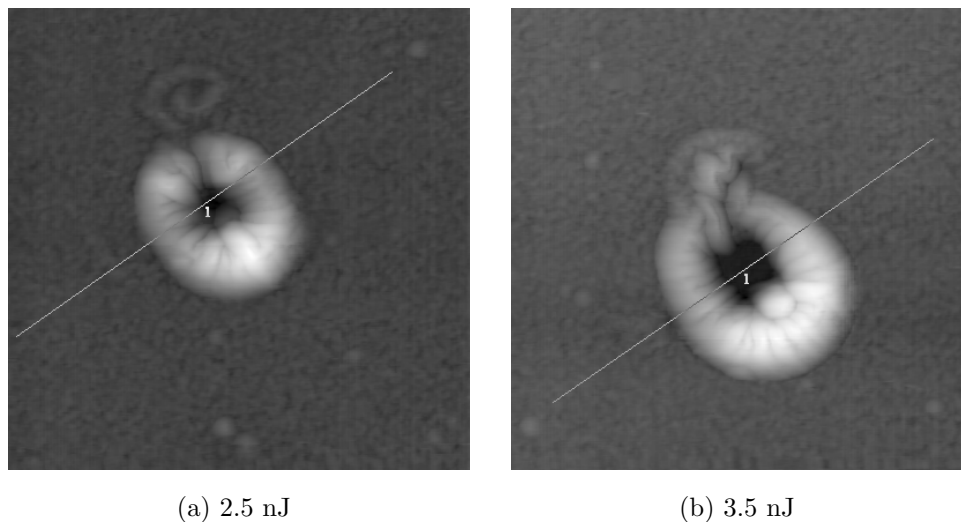
Figure 2.4: AFM images of ablation craters just above the ablation threshold for 400 fs ablation in air; (a) 2.5 nJ and (b) 3.5 nJ.
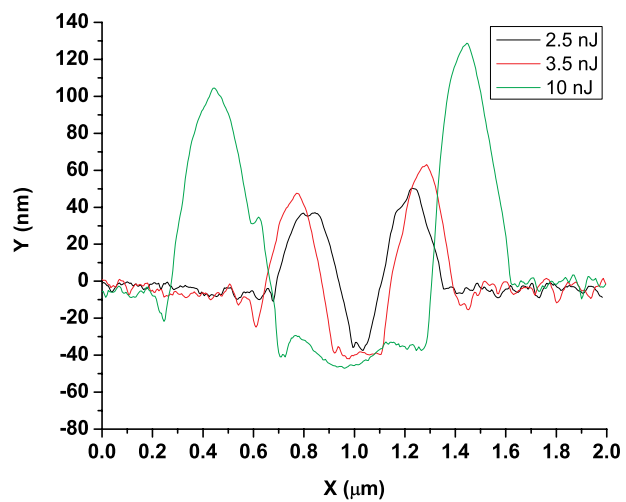
Figure 2.5: Crater cross-sections shown in Fig. 2.4 for 2.5, 3.5 and also 10 nJ pulse energies.

The focused $1/e^2$ laser spot size using the 0.85 NA lens is approximately $\lambda/NA \sim$ 500 nm for $\lambda = 400$ nm. Plots of the crater inner and outer diameters vs. pulse energy for the 0.85 NA lens in air are shown in Fig. 2.6.

400 ps pulses have a 300 nm crater inner diameter with complete film removal. For 6 ns pulses the 18 nJ case gave 400 nm resolution but was only a few nm deep and 20 nJ gave 25 nm film removal with a 600 nm crater inner diameter. The 130 nm inner diameter resolution shown in Fig. 2.5 with complete film removal for 400 fs pulses is 25 percent of the estimated $1/e^2$ spotsize. However, the repeatability of the film removal was poor for energies below 3.5 nJ where a crater inner diameter of 260 nm formed.

Lines were also written in air and vacuum by translating the sample 0.2 microns between shots. The increased amount of material removed compared to single shot ablation highlighted the advantages of working in a vacuum environment which offers less resistance to the expansion of the heated material and resulted in less debris on the surface. Sample AFM images shown in Fig. 2.7 (a) were obtained without ultrasonic cleaning of the sample when ablating in vacuum. A cross-section of the surface is also shown in Fig. 2.7 (b) and shows the high quality of the substrate surface in the ablated area. A mean roughness of 2 nm was measured from the AFM images for the ablated lines for pulse energies in the 'clean ablation' range.

A comparison of the ablated line surface quality for 4 ps and 6 ns pulses at 40-45 percent over the ablation threshold is shown in Fig. 2.8. The mean roughness of the 6 ns pulse is 13 nm while it is 2 nm for the 4 ps case, again highlighting the much smaller range of pulse energies where film ablation without substrate damage can occur for ns pulses.

For single-shot 6 ns pulses at 18 nJ, a shallow crater of less than 10 nm was made. When creating lines with multiple-shots at the same pulse energy, complete
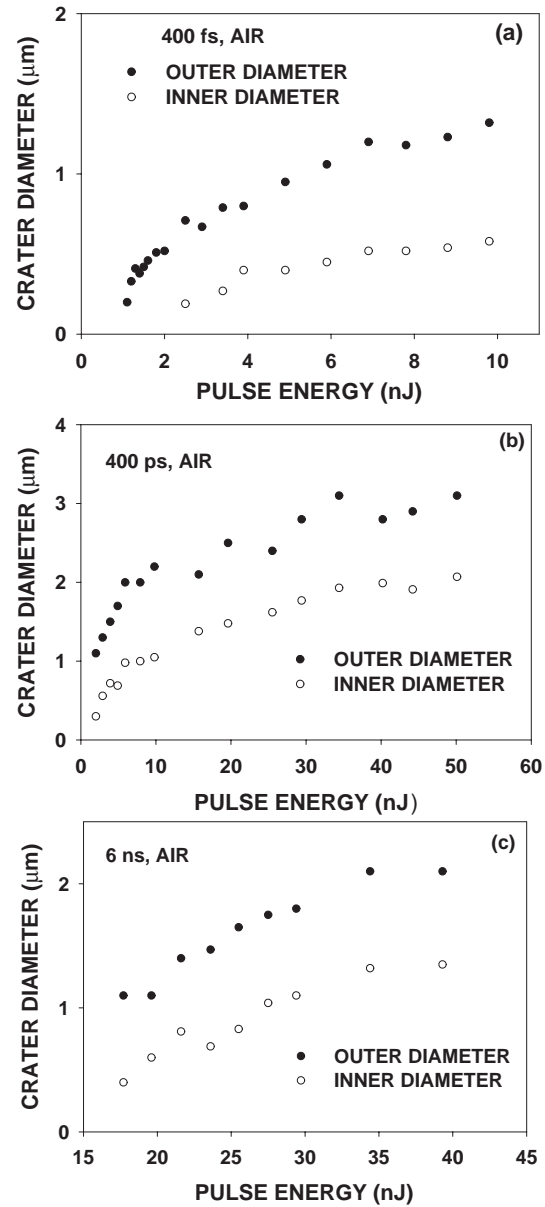
Figure 2.6: Crater inner and outer diameters vs. pulse energy for (a) 400 fs, (b) 400 ps, and (c) 6 ns pulse widths in air. Note the range of pulse energy where no inner diameter is formed for the 400 fs case. This pulse energy range is where the film surface is raised and will be discussed in more detail in the next section covering nanostructuring.

film ablation occurred as seen in the AFM image and cross-sections in Fig. 2.9. But even at this pulse energy, portions of the line had isolated spots of damage as seen in the Profile 1 cross-section in Fig. 2.9(b). A 400 nm inner diameter of the line was achieved in this case as Profile 2 in Fig. 2.9(b) shows.

2.3.2 Nanostructuring of Al Films

Fig. 2.10 shows a diagram of nanobump and nanojet features which have been observed after single shot 30 fs laser excitation of gold at fluences just above the damage threshold.[3] Research on the physical mechanisms of nanobump/nanojet formation is also an active area. Smooth nanobumps have been observed at lower fluences without a nanojet feature, and have been modeled as plastic deformation of the film which occurs without melting.[4] As fluence is increased, the central area of the film (with the highest temperature for a gaussian spatial laser energy distribution) undergoes melting. From volumetric considerations, the gold nanobumps and nanojets must be hollow structures. A hollow nanojet may form when the molten material continues to travel while the unmolten film is slowing. The flowing molten material cools into the nanojet for low enough fluences or becomes ejected at higher fluences.

Raised surface structures were noted on Al film for 400 and 600 fs pulses in air and for 300 fs pulses at 5 mtorr. For 4 ps pulses, no bump formation occurred for a pulse energy just 26 % below the pulse where clean ablation occurred, while the 400 fs data had repeatable raised surfaces for pulse energies from 40–70 % below the 3.5 nJ pulse energy where repeatable clean ablation began. If nanobumps/nanojets can be created with ps duration pulses, the range of fluence where this occurs is much smaller than for fs pulses.

For fs pulses, pulse energies just above the damage threshold produced raised surface features on the Al film shown in Fig. 2.11 with corresponding surface profiles

(a) AFM image.

(b) Cross-section from (a).
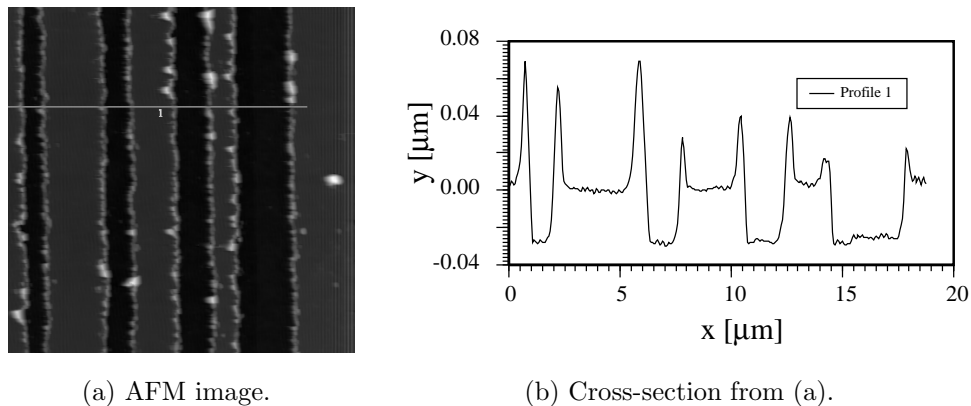
Figure 2.7: (a) AFM image of ablated lines for 4 ps pulses in vacuum and (b) cross-section shown in (a). Pulse energies used for each line are from left to right: 7, 8, 9, and 10 nJ.
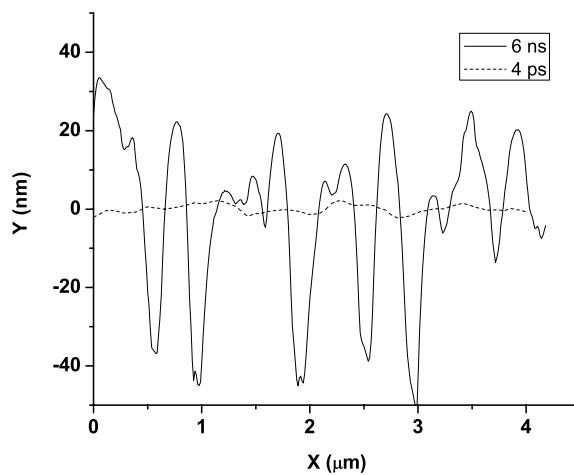
Figure 2.8: SiO_2 substrate profiles after Al film ablation of a line at 40-45 percent over the ablation threshold for 4 ps and 6 ns laser pulse widths. Mean roughness is 13 nm for the ns case and 2 nm for the ps case. Pulse energies are 9.8 nJ for 4 ps pulses and 26 nJ for 6 ns pulses.

(a) AFM image of line.

(b) Cross-sections from AFM image.
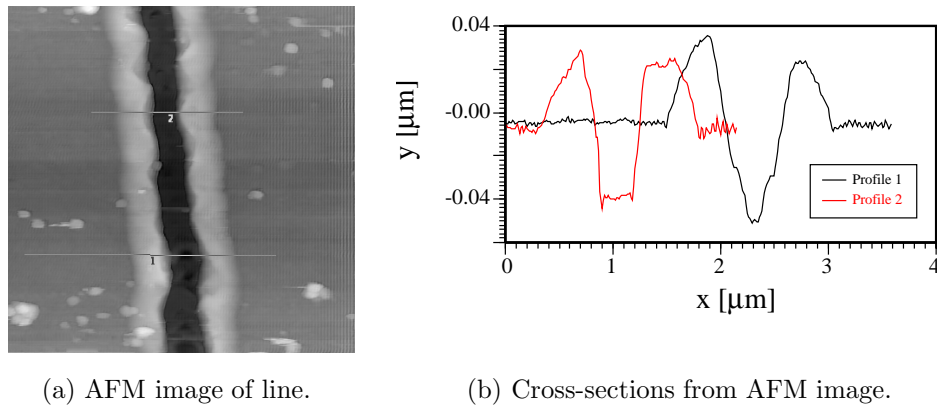
Figure 2.9: (a) AFM image of line made with 18 nJ, 6 ns pulses at 760 torr. (b) cross-sections indicated in the AFM image. Isolated melting of the substrate occurred as shown in Profile 1 in (b).
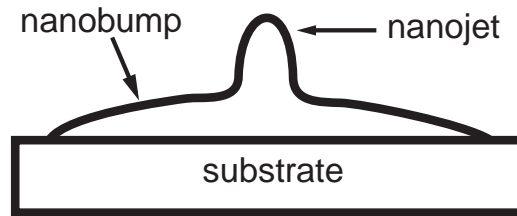
Figure 2.10: Diagram of nanobump and nanojet created by single pulse fs laser irradiation of Au film just above the damage threshold.

of the selected cross-sections shown in Fig. 2.12. An initial ring-like structure with a depression in the center at 1.1 nJ transforms into a central bump which grows in height as pulse energy increases. A feature with a steeper slope protrudes from the center of the nanobump and can be resolved for pulse energies above 1.6 nJ and can be seen in the 1.8 nJ profile in Fig. 2.12. The trapezoidal structure for the 1.8 nJ structure in Fig. 2.11(d) was later determined to be an image artifact of the high-aspect ratio of the nanojet and the 35 degree sidewall angles of the silicon nitride AFM probe used.

To minimize the distortions caused by high aspect-ratio features such as a nanojet, a silicon AFM probe with higher sidewall angles than the silicon nitride probe used

(a) 1.1 nJ

(b) 1.2 nJ

(c) 1.5 nJ

(d) 1.8 nJ
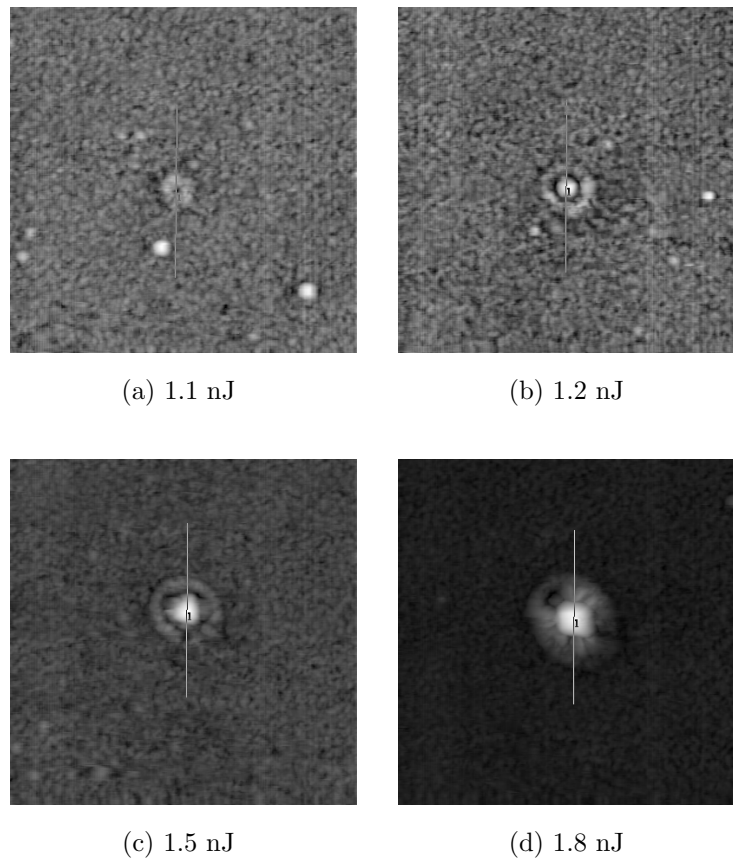
Figure 2.11: AFM images of raised surface features produced with 400 fs pulses at different pulse energies in air.
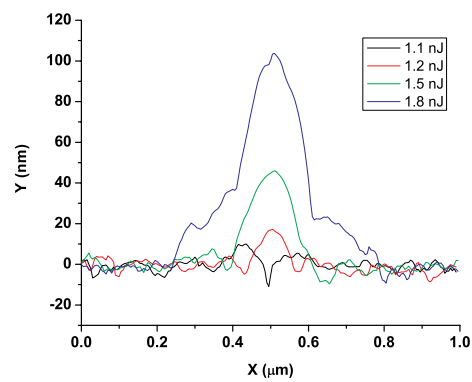
Figure 2.12: Bump profiles from cross-sections indicated in Fig. 2.11 as pulse energies vary.
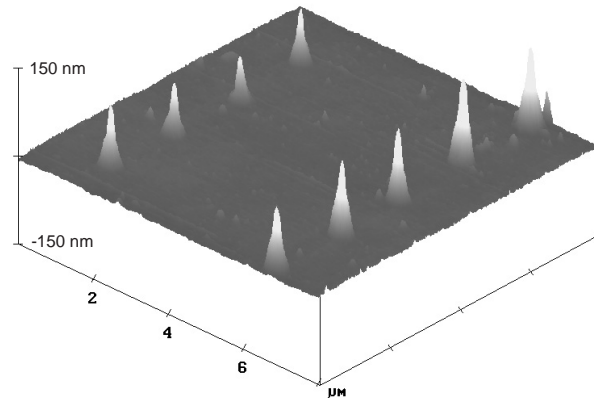
Figure 2.13: Nanoscale deformation of 20 nm Al film on fused silica created using 400 fs laser pulses. Laser pulse energy was 1.1 nJ for the far row and 1.2 nJ for the near row.

previously was used to obtain more AFM images in Fig. 2.13 and Fig. 2.14. Note that these images are not in the same location of the laser scanned sample and the laser focus has changed slightly compared to the previous AFM images due to the 550 nm depth of field of the lens used and imperfect leveling of the sample. The repeatability of the process is demonstrated in the AFM image in Fig. 2.13 for 1.1 and 1.2 nJ pulse energies. The nanojet formation can be more clearly resolved in the AFM image and profile in Fig. 2.14. The nanojet has a diameter of about 200 nm, similar to the nanojet sizes observed for gold. Radial variations of the nanobump height are also observed in Fig. 2.14. Radial variations in TEM images of ns laser-melted and resolidified free-standing Al films have been attributed to recrystallization effects as the Al resolidifies from the outer edge inward and may be the explanation of this feature.[12]

Fig. 2.15 shows the structure height vs. pulse energy for the energy range where good repeatability of the process occurred. A relative standard deviation of 10 % was typical for the heights of the structures for a given pulse energy. As pulse energy increases above 2 nJ, the repeatability of the bump creation process becomes poor
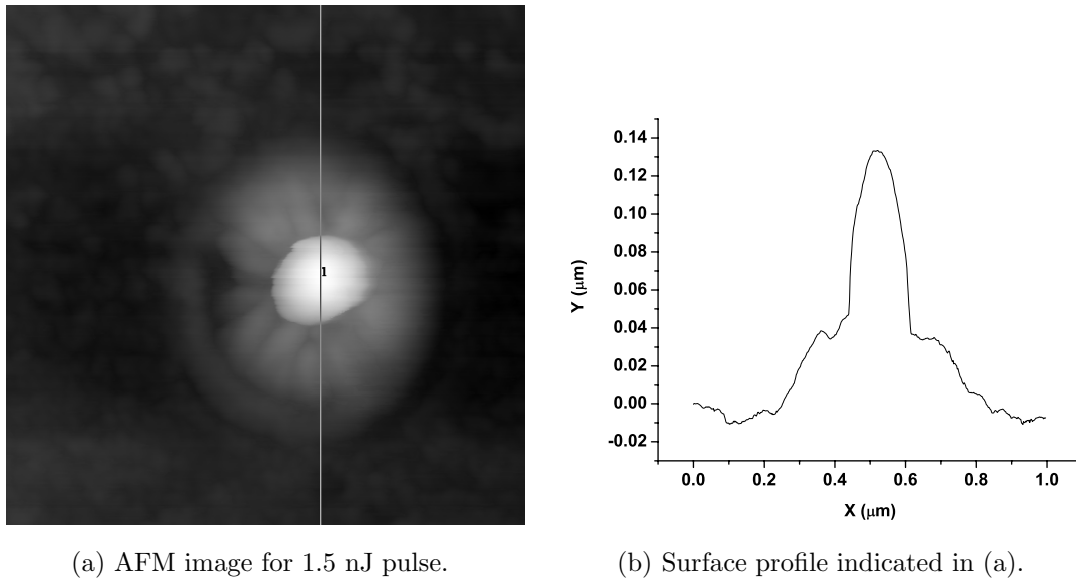
(a) AFM image for 1.5 nJ pulse.   (b) Surface profile indicated in (a).

Figure 2.14: (a) AFM image and (b) surface cross-section of nanobump/nanojet feature created with 400 fs, 1.5 nJ pulse.

until 3.5 nJ when a repeatable ablation crater begins. This lack of repeatability is presumed to be related to the start of the disintegration of the nanojet feature.

Experiments using a larger laser spotsize were performed with two purposes in mind. First to compare nanostructures made with a significantly larger spotsize with previous nanobumps/nanospikes and secondly, for improved accuracy in damage threshold measurements which will be discussed in the next section. Three trials with pulsewidths of 250 fs, 300 fs and 2 ps were performed and Fig 2.16 shows AFM images of the 250 fs damage for three fluences just above the damage threshold and one above the ablation threshold. Three common features occurred in all trials at fluences between the damage and ablation thresholds. First, a central raised feature forms just above the damage threshold as seen in Fig. 2.16(a),(b) and (c). A linear feature with a peak height near the center of the spot and oriented along the long axis of the elliptical damage spot occurs just above the damage threshold as seen in the 94 and 109 mJ/cm^2
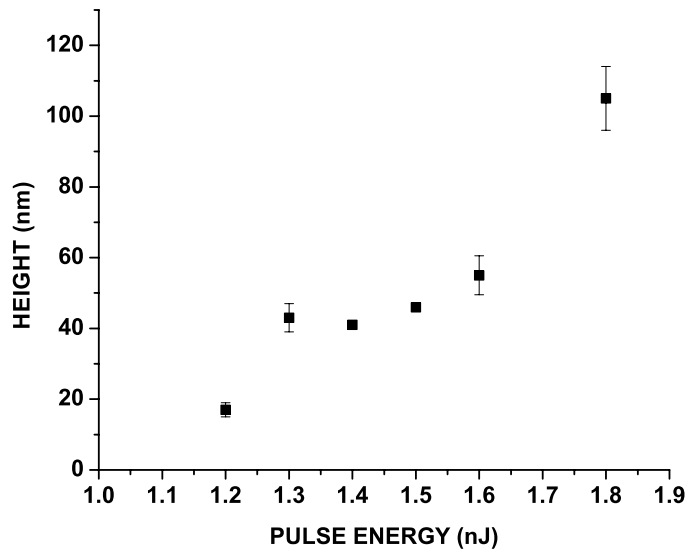
Figure 2.15: Structure heights vs. pulse energy for the range of energies where repeatable structures occurred.

images. The central protrusion then becomes circular as fluence is increased but still below the ablation threshold as seen in Fig. 2.16(c). The maximum height of this central raised feature is similar to that observed with smaller laser spotsizes, 150-170 nm for 109 and 125 mJ/cm^2. As fluence is increased, ablation occurs at the center of the damage spot as seen for the 140 mJ/cm^2 case in Fig. 2.16(d). No crater developed on the substrate up to the limits of fluence applied, more than 5 times the ablation threshold. The second and third features are ripples that extend radially from the center raised feature and an outer raised rim of material. These are observed in Fig. 2.16(a),(b) and (c). The ripples appear to become more ordered as fluence is increased while the spatial period of the ripples decreases with fluence. Radial ripples also form for smaller laser spotsizes as seen in Fig. 2.14. The outer rim height for large spotsizes increased with fluence and had a maximum height of 50 nm for 125 mJ/cm^2. Reflection and transmission optical microscopy show enhanced transmission and reduced reflectivity in a ring which appears to correspond with the raised rim

feature seen in AFM. Fig 2.17 shows optical microscope images for the 250 fs large spotsize damage. An outer circular ring with enhanced transmission can be seen at all fluences in Fig 2.17(a). Enhanced transmission and reduced reflection at the laser damage sites also occurred for the small spotsizes investigated previously. The enhanced transmission implies either a local thinning or rupture of the aluminum film at these sites or a possible rupture of the protective oxide, leading to oxidation of the aluminum underneath.

2.3.3 Al Film Damage Threshold

One of the first models to give good agreement with experimentally measured damage thresholds of metal films was developed by Matthias.[13] The model used the optical properties of the film, film thickness and thermal properties of both the film and substrate to model the change in threshold as film thickness varies. For ns pulses and substrates with poor thermal conduction, the film damage threshold scaled linearly with the film thickness until reaching a thickness which was equal to the thermal diffusion length of the film, $L_{th} = (2D\tau_L)^{1/2}$, where D is the diffusivity and τ_L is the laser pulsewidth. The damage threshold then became constant for thicker films. This model is a one-dimensional diffusion model where the heated depth of the film is limited to the film thickness for thicknesses less than L_{th}.

A nonequilibrium situation can occur between the electrons and lattice of a metal for laser pulses shorter than about 1 ns duration. The electrons are heated first and then energy is transferred to the lattice on a time scale of typically a few ps for metals. The concept of thermal diffusion assumes an equilibrium between the electron and lattice temperatures and becomes invalid for pulses which are shorter than the characteristic time of energy transfer between the initially laser-excited electrons and phonons. Corkum first described the change in the scaling of the damage threshold

(a) 94 mJ/cm^2

(b) 109 mJ/cm^2

(c) 125 mJ/cm^2
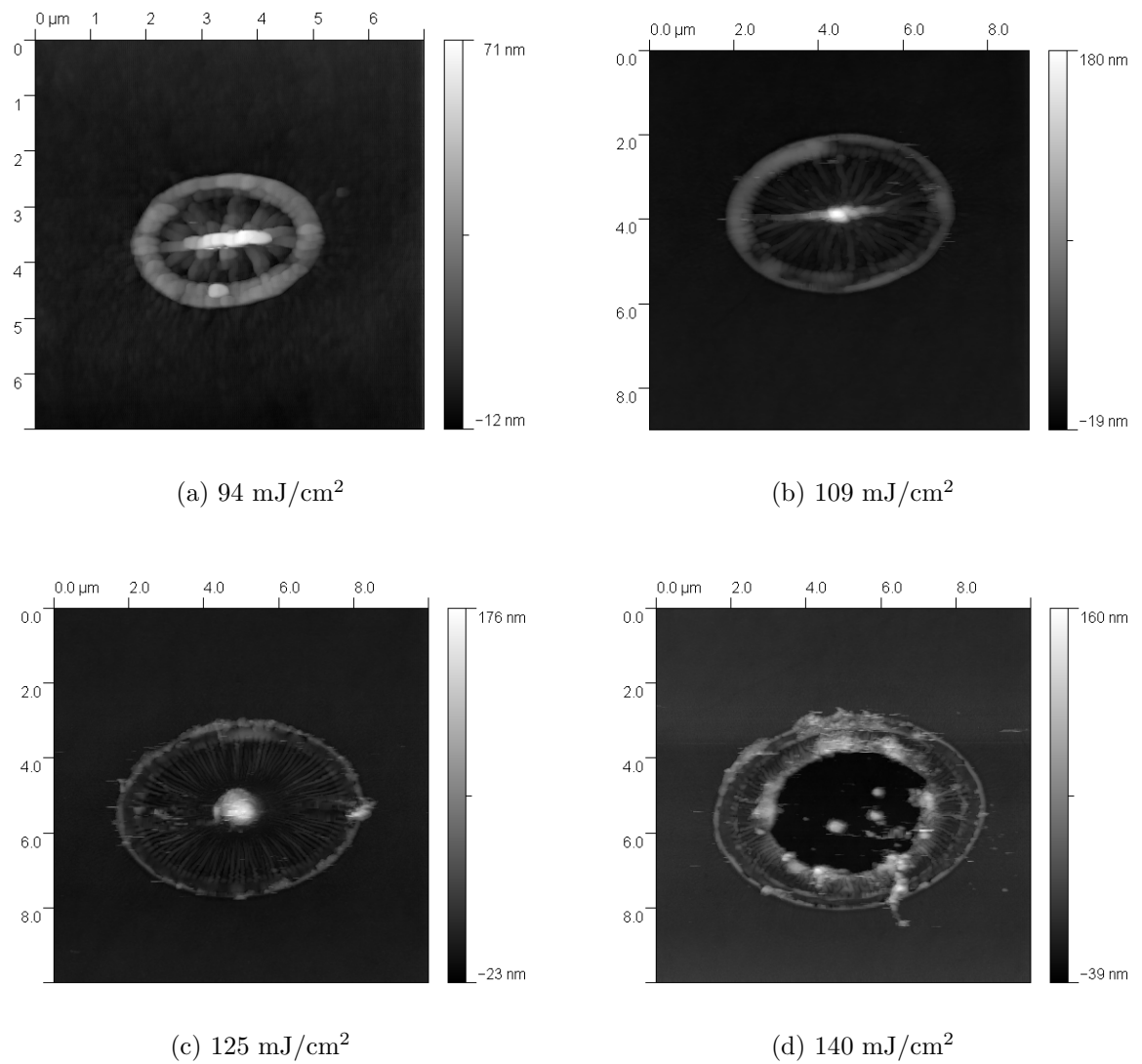
(d) 140 mJ/cm^2

Figure 2.16: 250 fs AFM images of three fluences above the damage threshold and one above the ablation threshold at 140 mJ/cm^2. Note the change in scaling between images.
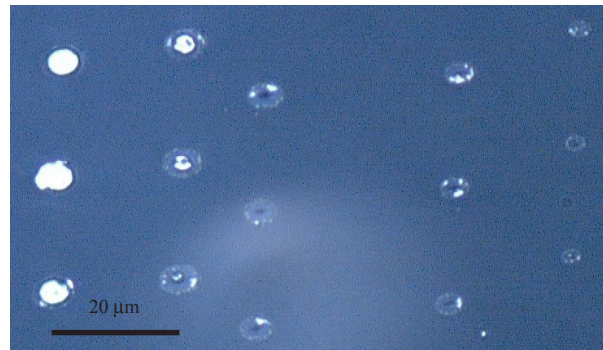
(a) Transmission

(b) Reflection

Figure 2.17: 250 fs optical transmission and reflection microscopy of three fluences above the damage threshold and two fluences above the ablation threshold. Each column of three damage spots is at a fixed fluence in the image. Fluences are from left to right: 155, 140, 125, 109 and 94 mJ/cm^2. Note enhanced transmission near the edge of the damage area for low fluences. The enhanced transmission area becomes centralized above the ablation threshold at 140 mJ/cm^2. Note that the approximately 20 micron diameter ring near the lower central region of the tranmission image is an image artifact.

versus laser pulse width in bulk metals.[14] For pulses shorter than a critical pulse width, the damage threshold deviates from scaling as the square root of the laser pulse width as is expected for one-dimensional thermal diffusion. For pulses shorter than a critical pulse width the heated depth when electrons and lattice reach equilibrium is expected to be relatively constant and determined by diffusion of nonequilibrium electrons. The critical pulsewidth, τ_c, and critical heated depth, L_c, for pulses shorter than τ_c, can be expressed as:[14]

$$\tau_c = \left(\frac{8}{\pi}\right)^{1/4} \left(\frac{C_l^3}{A_e T_m g^2}\right)^{1/2} \tag{2.1}$$

$$L_c = \left(\frac{128}{\pi}\right)^{1/8} \left(\frac{K_0^2 C_l}{A_e T_m g^2}\right)^{1/4} \tag{2.2}$$

Here C_l is the lattice heat capacity, A_e is the electronic specific heat coefficient, T_m is the melting temperature, g is the electron-phonon coupling parameter and K_0 is the thermal conductivity.

It is desirable to have a model to predict the damage threshold of metal films which would be applicable for pulses shorter than τ_c, where the concept of thermal diffusion is no longer correct. For pulses shorter than τ_c, the effective heated depth becomes the smaller of either L_c or the film thickness, assuming negligible electron transport into the substrate. Assuming one-dimensional diffusion the energy density in the film is simply the absorbed fluence divided by the smaller of the film thickness or the critical heated depth. Equating this energy density to the energy density needed to raise the film to the melting point plus the heat of fusion and rearranging gives the following expression for damage fluence, F_d, for laser pulsewidths less than the critical pulsewidth:

$$for \ \ d < L_c \qquad F_d = \frac{\Delta T}{A(d)} \left[\rho_f c_f d\right] + \frac{H_f d}{A(d)} \tag{2.3}$$

$$for \ \ d \geq L_c \qquad F_d = \frac{\Delta T}{A(d)} \left[\rho_f c_f L_c \right] + \frac{H_f L_c}{A(d)} \qquad (2.4)$$

where ΔT is the temperature rise from the initial temperature to T_m, d is the film thickness, $A(d)$ is the film absorption, ρ_f and c_f are respectively, the density and heat capacity of the film, and H_f is the heat of fusion of the film.

Equations 2.3 and 2.4 assume one-dimensional energy transport, requiring that the laser spot size be much greater than the heated depth. The assumption that damage occurs at the equilibrium melting point is also made in these equations and heating rate is unimportant, as has been assumed in other damage threshold models for ductile metals.[15] The lattice heating time caused by a subpicosecond laser, $\tau_l = C_l/g$, is approximately 5 ps for aluminum, where C_l is the lattice heat capacity and g is the electron-phonon coupling parameter.[16]

Güdde has modeled the damage threshold vs. thickness for gold and nickel films.[15] Using the film lattice specific heat as a fitting parameter, values 3 times smaller than the bulk were derived. This result was suggested to be due to an incomplete excitation of all phonon modes on the ps time scale needed for melting to take place.

For damage threshold calculations, measurements of the laser spot diameter on the sample surface were made by both the scanning knife edge technique[17] and by a fitting procedure which fits the measured damage radius on the sample vs. pulse energy to a theoretical model to determine both the damage threshold and laser spot-size simultaneously.[18] The diameter of the damage crater as a function of pulse energy for a spatially Gaussian beam can be expressed as:

$$d(E) = \frac{d_0}{\sqrt{2}} \sqrt{\ln(F_0/F_d)} \qquad (2.5)$$

where $F_0 = \frac{2E}{\pi r_{0x} r_{0y}}$ or $F_0 = \frac{2E}{\pi r_0^2}$ is the peak fluence for elliptical and circular Gaussian beams, respectively, E is the laser pulse energy, $d(E)$ is the diameter of the

damaged area, d_0 is the $1/e^2$ beam diameter, F_d is the peak damage threshold fluence, r_{0x}, and r_{0y} are the $1/e^2$ radii for an elliptical beam and r_0 is the $1/e^2$ radius for a circular beam.[19,20] For elliptical Gaussian beams, $d(E)$ and d_0, are characteristic of each axis of the beam. A single equation was fit to the damage spot dimensions for circular Gaussian beams while two equations were fit simultaneously for each axis of elliptical beams. Further details of the spot size determination method by fitting damage radius vs. pulse energy are in Appendix B.

The fitting procedure was applied to small spot-size experiments to determine the damage fluence. The damage threshold calculated in this manner for sub-ps pulses varied by a factor of three from 25-72 mJ/cm^2. The determination of accurate damage threshold measurements is typically limited by the accuracy of the spot-size measurement. The one-dimensional model also requires a large spot-size to be able to ignore radial diffusion, making a larger spot more applicable for comparison with theory. To improve accuracy of the damage threshold measurement using large spot-sizes, the beam diameters found by the fitting procedure for large spot-sizes were compared with diameters determined with the scanning knife edge technique and agreement of the $1/e^2$ area was within 10%.

Fig. 2.18 shows the result of the fitting procedure for elliptical damage spots where a damage threshold of 84 mJ/cm^2 and $1/e^2$ beam radii of 5.2 and 7.5 microns were determined for the 20 nm Al film for a 250 fs pulse. The two lines in the graph represent the radius squared of the long and short axes of the elliptical damage spot and the x axis intercept determines the damage fluence. It should be noted that this fitting method to determine the damage threshold and beam diameter also assumes no radial diffusion of energy and was originally used with ps pulses. A summary of the three trials performed with the large spot size setup is shown in Table 2.3. Note that although the standard error reported for an individual fit is quite small,

the repeatibility from day to day for a given pulsewidth approaches 30%. Thus no significant differences in damage thresholds between the trials are observed as expected for pulses shorter than the critical pulsewidth. The values of the critical pulsewidth and critical heated depth for aluminum are calculated to be 34 ps and 81 nm respectively, using Eqs. 2.1 and 2.2 and parameter values listed in Table 2.1. Since the 20 nm aluminum film thickness is less than the critical heated depth of 81 nm for aluminum, Eq. 2.3 is applicable and gives a predicted damage threshold of 44 mJ/cm^2 using the experimentally measured absorption of 0.15 and parameters given in Table 2.1.
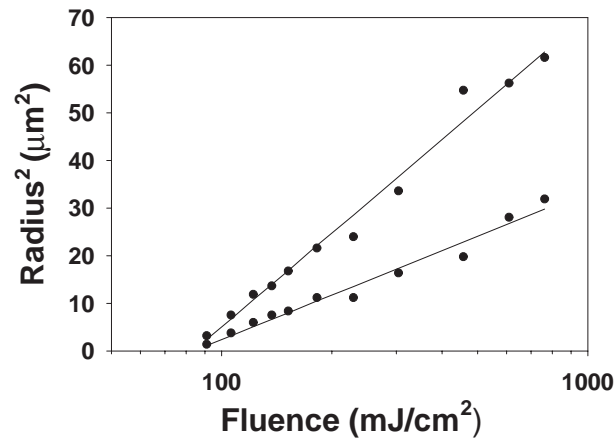
Figure 2.18: Fit of damage radii vs. peak fluence to determine 20 nm Al film damage threshold of 84 mJ/cm^2 for 250 fs pulse.

The experimental damage thresholds are 2–3 times higher than the theoretical value. This is a reasonable first order estimate and the model's inherent simplicity makes it quite useful. Three mechanisms which would increase the damage threshold are discussed. First, the oxide covering the Al film is not included in the model and additional energy is required to bring the temperature of the aluminum oxide to its melting point of 2327 °K. Secondly, consideration of the loss of hot electron energy to the oxide and substrate during the electron equilibration process may also

Table 2.3: Summary of Al film damage threshold results. The parameters d_0 ($1/e^2$ spotsize diameter) and F_d (peak damage fluence and standard error) obtained from fits of measured crater dimensions to Eq. 2.5 are given. Two values are listed for d_0 for each axis of the elliptical beams.

Pulsewidth	$d_0(\mu\text{m})$	$F_d(\text{mJ/cm}^2)$
250 fs	10.4,15.0	84 ± 2
300 fs	9.2,12.3	100 ± 5
2 ps	9.4,12.0	117 ± 6

become increasingly important as metal films become thinner. Transient thermoreflectance measurements of 20 nm gold films have shown that as electron temperatures increase energy losses to the substrate from electron-boundary scattering also increase.[21] Adding this loss mechanism which occurred below damage threshold improved agreement with the theoretical electron-phonon coupling parameter for gold. The final mechanism which could increase the damage threshold is the increase in the specific heat for thin films relative to bulk material. It is known that thin film thermophysical properties can be different from bulk properties. Enhanced specific heat capacity has been measured in thin Al films less than a micron thick using a microcalorimeter.[22] 1150 nm thick films agreed with bulk values and an increase of specific heat capacity by 2–3 times the bulk value was measured at 420 K for a 40 nm film. This enhanced specific heat of the thin film would also raise the damage threshold from calculations using the bulk value. But there is disagreement in the literature regarding the change in specific heat vs. film thickness. Microcalorimeter measurements of aluminum thin films from 13.5–370 nm found a *decrease* of less than 10% in specific heat as film thickness decreased in this film thickness range.[23]

The damage threshold model assumption that the absorption is constant up to the damage threshold is supported by experiments measuring absorption of 400 nm, 50 fs pulses in 500 nm thick Al films vs. laser intensity. Absorption has been measured to be

approximately constant up to an absorbed fluence of 70 mJ/cm^2, 5 times greater than the 14 mJ/cm^2 absorbed fluence at damage threshold in this work.[24] Other studies of Al self-reflectivity vs. laser intensity also show the same trend at wavelengths far from the 800 nm parallel band absorption region. Experiments using 400 fs, 308 nm[25] and 120 fs, 620 nm[26] lasers also show an almost constant Al self-reflectivity until 10^{12} and 10^{13} W/cm^2, or expressed as absorbed fluence, 40 and 240 mJ/cm^2, again greater than this work and justifying the constant absorption assumption. For the spectral region near 800 nm where parallel band absorption occurs in Al, the assumption of constant absorption up to the damage threshold would have to be reexamined as a decrease in absorption as intensity increases has been noted.[24] The time scale of the sub-ps pulse allows the self-reflectivity contributions coming from lattice heating to be ignored and which have to be considered for longer pulses.[27]

A heat deposition depth of 170 nm has been inferred from Al damage threshold measurements using 400 nm, 130 fs pulses.[28] This depth is a factor of two higher than the critical heated depth calculated here using Eq. 2.2 and results from the use of an electron-coupling parameter which is a factor of five smaller than used in this work. There is a variation by a factor of seven in the value of the electron-phonon coupling parameter in the literature as noted in Table 2.4. The electron specific heat also has differences of about 30%.[8,29] The variation of these two parameters lead to changes in the critical pulseswidth, τ_c, (defined in Eq. 2.1) and critical heated depth, L_c. By varying these two parameters, minimum and maximum values are obtained for the critical pulse width and critical heated depth; 25 ps and 69 nm for large electron-phonon coupling parameter and 206 ps and 200 nm for the small value of electron-phonon coupling parameter. Even the case of the smallest (69 nm) critical heated depth calculated above is still larger than the 20 nm film thickness, so Eq. 2.3 which was used to calculate the damage threshold is still valid.

Table 2.4: Summary of electron-phonon coupling parameters for Al in the literature.

Electron-phonon coupling parameter ($Wcm^{-3}K^{-1}$)	Reference
3.1 x 10^{11} (Theoretical)	Rethfeld et al.[30]
5.7 x 10^{11} (Theoretical)	Hüttner et al.[29]
4.9 x 10^{11} (Theoretical) 0.8 x 10^{11} (Experimental)	Tas and Maris[8]
2.0–2.5 x 10^{11} (Experimental)	Hostetler et al.[31]

2.4 Conclusions

A large window of pulse energies exists where clean ablation of the 20 nm Al film can be obtained with minimal damage to the substrate for pulses shorter than 4 ps. This pulse energy range was a factor of 2.6-7.3 times the clean ablation threshold for pulses less than 4 ps and decreased with increasing laser pulse width to ≤1.2 for 6 ns pulses.

When using the technique of varying laser energy with a gaussian spatial distribution for Al films, there is a minimum ablation crater diameter. The minimum crater diameter obtained with complete ablation of the film was 130–260 nm for a 400 fs pulse. As pulse energy drops further, raised structures are formed. The fluence range just below ablation, where raised nanostructures are formed generated sub-micron structures which were 10's of nm high and grew with pulse energy. As fluence increased, sharp protrusions formed in the center of these bumps and height increased up to 150 nm.

The sub-ps laser damage threshold of 20 nm Al films was measured to be two to three times higher than a theoretical model which assumes an equilibrium melting temperature and bulk . Possible mechanisms for this discrepancy were proposed including electron energy losses to the substrate and Al thin film specific heat which is different than the bulk.

REFERENCES

1. R. Haight, D. Hayden, P. Longo, T. Neary, and A. Wagner, "MARS: Femtosecond laser mask advanced repair system in manufacturing," *J. Vac. Sci. Technol. B*, vol. 17, pp. 3137–3143, 1999.

2. P. P. Pronko, S. K. Dutta, J. Squier, J. V. Rudd, D. Du, and G. Mourou, "Machining of sub-micron holes using a femtosecond laser at 800 nm," *Opt. Commun.*, vol. 114, pp. 106–110, 1995.

3. J. Koch, F. Korte, T. Bauer, C. Fallnich, A. Ostendorf, and B. N. Chickov, "Nanotexturing of gold films by femtosecond laser-induced melt dynamics," *Appl. Phys. A*, vol. 81, pp. 325–328, 2005.

4. Y. P. Meshcheryakov and N. M. Bulgakova, "Thermoelastic modeling of microbump and nanojet formation on nanosize gold films under femtosecond irradiation," *Appl. Phys. A*, vol. 82, pp. 363–368, 1996.

5. E. D. Palik, ed., *Handbook of Optical Constants of Solids*. New York: Academic Press, 1985.

6. *American Institute of Physics Handbook, 3rd Ed.*, pp. 4–222. New York: McGraw-Hill, 1972.

7. S. Musikant, *Optical Materials: An introduction to selection and application*, p. 189. New York: Dekker, 1985.

8. G. Tas and H. J. Marris, "Electron diffusion in metals studied by picosecond ultrasonics," *Phys. Rev. B*, vol. 49, pp. 15046–15054, 1994.

9. E. D. Palik, ed., *Handbook of Optical Constants of Solids*. New York: Academic Press, 1985.

10. E. D. Palik, ed., *Handbook of Optical Constants of Solids II*. New York: Academic Press, 1991.

11. *http://en.wikipedia.org/wiki/Aluminium_oxide*.

12. O. Bostanjoglo and T. Nink, "Hydrodynamic instabilities in laser pulse-produced melts of metal films," *J. Appl. Phys.*, vol. 79, pp. 8725–8729, 1996.

13. E. Matthias, M. Reichling, J. Siegel, O. W. Käding, S. Petzoldt, H. Skurk, P. Bizenberger, and E. Neske, "The influence of thermal diffusion on laser ablation of metal films," *Appl. Phys. A*, vol. 58, pp. 129–136, 1994.

14. N. K. Sherman, F. Brunel, P. B. Corkum, and F. A. Hegman, "Transient response of metals to ultrashort pulse excitation," *Opt. Eng.*, vol. 28, pp. 1114–1121, 1989.

15. J. Güdde, J. Hohlfeld, J. G. Müller, and E. Matthias, "Damage threshold dependence on electron-phonon coupling in Au and Ni films," *Appl Surf. Sci.*, vol. 127–129, pp. 40–45, 1998.

16. S. Nolte, C. Momma, H. Jacobs, A. Tünnermann, B. N. Chickov, B. Welleghausen, and H. Welling, "Ablation of metals by ultrashort laser pulses," *J. Opt. Soc. Am. B*, vol. 14, no. 10, pp. 2716–2722, 1997.

17. Y. Suzaki and A. Tachibana, "Measurement of the micron sized radius of gaussian laser beam using the scanning knife edge," *Appl. Opt.*, vol. 14, pp. 2809–2810, 1975.

18. J. M. Liu, "Simple technique for measurements of pulsed gaussian-beam spot sizes," *Opt. Lett.*, vol. 7, pp. 196–198, 1982.

19. D. von der Linde and H. Schüler, "Breakdown threshold and plasma formation in femtosecond laser-solid interaction," *J. Opt. Soc. Am. B*, vol. 13, no. 1, pp. 216–222, 1996.

20. C. A. MacDonald, A. M. Malvezzi, and F. Spaepen, "Picosecond transient reflectance measurements of crystallization in pure metals," in *Beam-Solid Interactions and Phase Transformations* (H. Kurz, G. L. Olson, and J. M. Poate, eds.), vol. 51 of *Materials Research Society Symposium Proceedings*, (Warrendale, PA), pp. 277–282, Materials Research Society, 1986.

21. P. E. Hopkins and P. M. Norris, "Substrate influence in electron-phonon coupling measurements in thin Au films," *Appl. Surf. Sci.*, vol. 253, pp. 6289–6294, 2007.

22. Y. Jun, T. Zhen-An, Z. Feng-Tian, W. Guang-Fen, and W. Li-Ding, "Investigation of a microcalorimeter for thin-film heat capacity measurement," *Chinese Phys. Lett.*, vol. 22, pp. 2429–2432, 2005.

23. Q. Song, Z. Cui, S. Xia, and S. Shen, "An ac microcalorimeter for measuring specific heat of thin films," *Microelectronics Journal*, vol. 35.

24. D. Fisher, M. Fraenkel, Z. Henis, E. Moshe, and S. Eliezer, "Interband and intraband (drude) contributions to femtosecond laser absorption in aluminum," *Phys. Rev. E*, vol. 65, pp. 016409–1–016409–7, 2001.

25. H. M. Milchberg and R. R. Freeman, "Studies of hot dense plasmas produced by an intense subpicosecond laser," *Phys. Fluids B*, vol. 2, no. 6, pp. 1395–1399, 1990.

26. M. K. Grimes, A. R. Rundquist, Y. S. Lee, and M. C. Downer, "Experimental identification of vacuum heating at femtosecond-laser-irradiated metal surfaces," *Phys. Rev. Lett.*, vol. 82, no. 20, pp. 4010–4013, 1999.

27. K. C. Lee, C. S. Chan, and N. H. Cheung, "Pulsed laser-induced damage threshold of thin aluminum films on quartz: Experimental and theoretical studies," *Journal of Applied Physics*, vol. 79, no. 8, pp. 3900–5, 1996.

28. C. Guo, G. Rodriquez, A. Lobad, and A. J. Taylor, "Structural phase transition of aluminum induced by electronic excitation," *Phys. Rev. Lett.*, vol. 84, no. 19, pp. 4493–4496, 2000.

29. B. Hüttner and G. Rohr, "On the theory of ps and sub-ps laser pulse interactions with metals I. Surface temperature," *Appl. Surf. Sci.*, vol. 103, pp. 269–274, 1996.

30. B. Rethfeld, A. Kaiser, M. Vicanek, and G. Simon, "Femtosecond laser-induced heating of electron gas in aluminum," *Applied Physics A [Suppl.]*, vol. 69, pp. S109–S112, 1999.

31. J. L. Hostetler, A. N. Smith, D. M. Czajkowsky, and P. M. Norris, "Measurement of the electron-phonon coupling factor dependence on film thickness and grain size in Au, Cr and Al," *Appl. Opt.*, vol. 38, pp. 3614–3620, 1999.

Chapter 3

Femtosecond Laser Micromachining of Quartz

Abstract

Slots are micromachined in 75 μm thick crystalline quartz samples using 50 femtosecond laser pulses in a vacuum of 10 mTorr. The processed area cut quality at the laser entrance and exit sides is examined by optical microscope and environmental scanning electron microscope. Cuts with a high quality laser entrance side without microcracking could be obtained for fluence ranges from 2.5-13 J/cm^2 while microcracking at the cut entrance is observed at 16 J/cm^2. Damage on the exit side of the sample was observed within a distance of 50 μm from the center of the cut and runs parallel to the laser cut.

3.1 Introduction

Ultrafast lasers are an effective tool for micromachining many materials including op-
tically transparent dielectrics. Free carriers are efficiently generated by either multi-
photon or Zener ionization and additional carriers are created by avalanche ionization
for laser intensities above the breakdown threshold.[1–5] The material rapidly increases
absorption as the laser intensity exceeds the breakdown threshold which provides a
means for controlled ablation. Laser machining shallow grooves in glasses with high
quality has been demonstrated.[6,7] However, few papers have focused on cutting slots
or drilling holes completely through these materials and undesirable damage such as
microcracking and chipping has been noted at the edges of the laser processed region
for these brittle materials. Microcracking at the entrance and exit holes was observed
in high aspect ratio hole drilling in fused silica,[8] while laser exit side damage was
noted in fs laser cutting and drilling of glasses.[9–11] The use of a liquid to enhance
the material removal process in the fabrication of high aspect ratio channels has also
been investigated.[12] In this process, a tightly focused laser beam is scanned over the
ablation area with a liquid in contact with the laser ablated surface. This study
investigates micromachining slots in 75 μm thick crystalline quartz using a focusing
lens with a large depth of field relative to the thickness of the material. The impact
of laser processing parameters on the quality of the entrance and exit of the cuts are
of main interest in this work.

3.2 Experimental

The laser system consists of a regenerative laser amplifier system based on chirped
pulse amplification. Low energy seed pulses are provided by a mode-locked Ti:sapphire
oscillator (Kapteyn-Murnane Labs) which is pumped by a diode-pumped cw visible

laser (Spectra-Physics, Millennia Vs). Pulses are amplified in a Ti:sapphire regenerative amplifier system (Spectra-Physics, Spitfire) pumped by an intracavity frequency doubled, diode-pumped Nd:YLF laser (Spectra-Physics, Evolution X). 800 μJ pulses are generated at a center wavelength of 800 nm at 1000 Hz repetition rate.

The stretcher and compressor of the regenerative amplifier are adjusted to give a 50 fs laser pulsewidth as measured using a Positive Light Frequency-Resolved Optical Gating system. A beam-profiling camera (WincamD, Dataray) is used to verify that the laser output is Gaussian.

Neutral density filters were used to vary the laser power. The laser power after the neutral density filter is measured using a calibrated photodiode with attenuating filter. The beam is focused on the sample at normal incidence using a plano-convex fused silica lens of 75 mm focal length. The sample surface was monitored by imaging reflected light from an illumination source onto a CCD camera using the same lens. Computer controlled motion of the sample was performed with Melles Griot Nanomotion translation stages providing XYZ motion. Translation speed is adjustable from 5-2500 μm/sec. An electronically controlled shutter is used to control exposure on the sample and a small chamber with a fused silica window was attached to the XYZ translators and provides 10 mTorr vacuum.

Samples are polished AT-cut crystalline quartz, 75 μm thick and 6 mm in diameter made by M-Tron Industries. The damage diameter of the focused beam was measured as a function of pulse energy and fit to a function derived from Gaussian beam theory in order to determine the $1/e^2$ spot diameter used in calculating average fluence.[13]

Samples were examined as processed with an optical microscope in transmission mode and an environmental scanning electron microscope (ESEM) to determine cut width and depth and the amount of microcracking and other damage at the entrance and exit sides. Laser cuts were performed at the edge of the sample to allow examination of the cut cross-section if desired.

3.3   Results and discussion

The focal position giving the smallest spot was determined by varying the sample position in 100 μm increments and finding the narrowest line width. 20 pulse exposures were then made at a fixed position at this focus and the damage diameters measured. A $1/e^2$ beam diameter of 17 μm and a 20 pulse damage threshold of 1 J/cm^2 were derived from this data. This focal position was used in all work reported here except when noted otherwise.

ESEM images of selected 20 shot laser entrance and exit side damage are shown in Fig. 3.1. The increase in the entrance side damage diameter as fluence is increased is characteristic of Gaussian beams just above the damage threshold. Slight chipping is sometimes observed surrounding the entrance holes. Exit side damage occurred for fluences above 5.4 J/cm^2 and was not observed for 3.2 and 2.0 J/cm^2. A morphology typical of spalling with extensive chipping is observed at the 16 J/cm^2 laser exit site. Smaller individual damage spots are observed for the lower fluence exit side images along with a larger area of contrast change which indicates a modification of the exit side surface.

Optical micrographs of groove cross-sections cut at the edge of the samples are shown in Fig. 3.2. Fig. 3.2(a) has varying number of passes at the lowest and highest fluences considered, 2.5 and 16 J/cm^2, respectively. An intermediate fluence of 5.4 J/cm^2 is shown in Fig. 3.2(b) The image is focused on the laser exit side of the sample in each case. Damage was observed on the laser exit side running parallel to the laser cut and approximately 50 μm from the center of the laser cut for the two higher fluences while no similar exit side damage was observed at 2.5 J/cm^2. This damage was also symmetric on either side of the laser cut as can be seen for the 5.4 and 16 J/cm^2 cuts. The maximum distance that the exit side damage extended from the
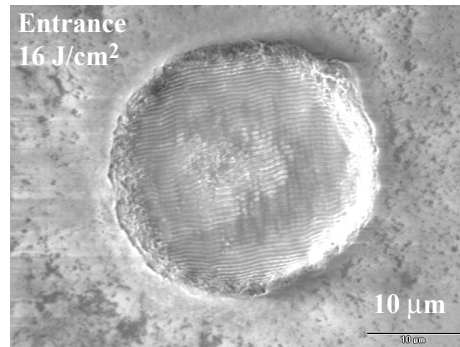
(a) Entrance side: 16 J/cm^2
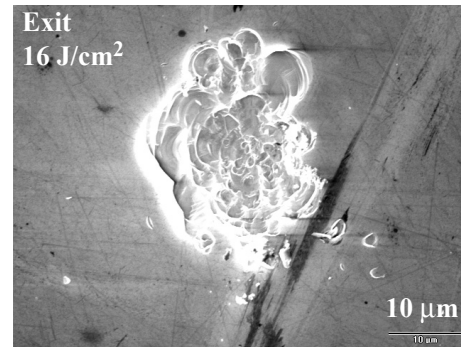
(b) Exit side: 16 J/cm^2
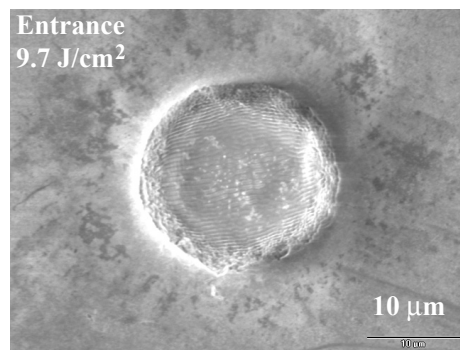
(c) Entrance side: 9.7 J/cm^2
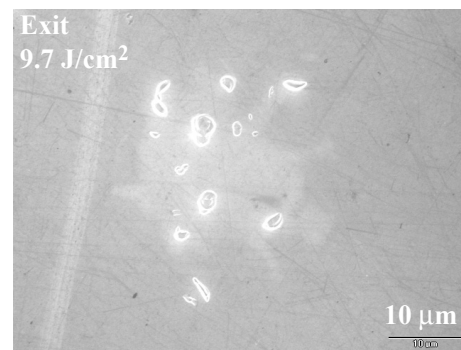
(d) Exit side: 9.7 J/cm^2
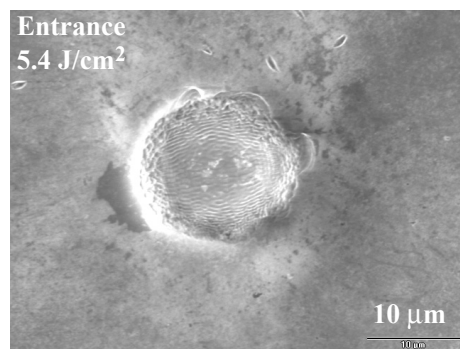
(e) Entrance side: 5.4 J/cm^2
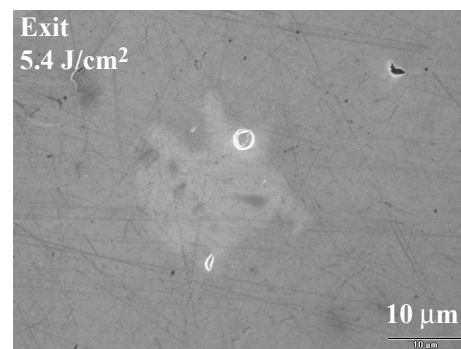
(f) Exit side: 5.4 J/cm^2

Figure 3.1: ESEM images of the laser entrance and exit sides of the quartz sample after 20 pulses at the fluence indicated.

center of the slot was 57 μm, measured for the 16 J/cm^2 case where contributions of the back side damage from adjacent cuts was absent. These images also show that the amount of backside damage increases with both the number of passes and fluence. The 10 pass cut in Fig. 3.2(b) is below the threshold number of passes required to generate the backside damage at this fluence since exit side damage is not seen to the right of this cut.
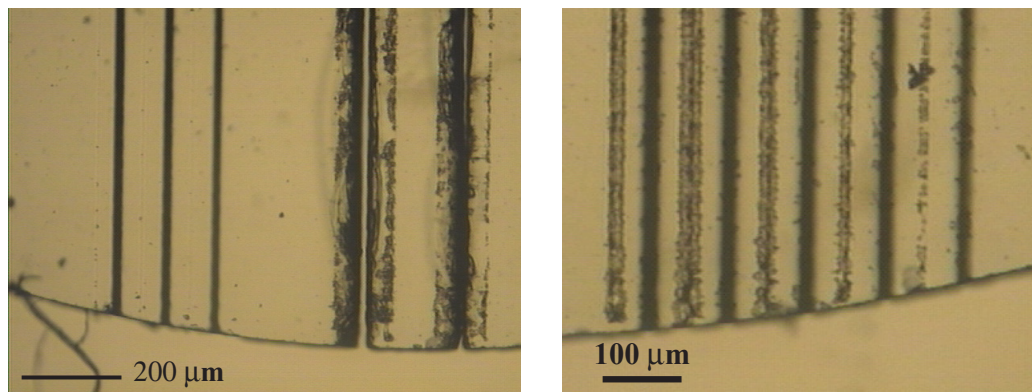
(a) From left to right: 2.5 J/cm^2 with 400, 200 and 40 passes.; 16 J/cm^2 with 100 and 20 passes.

(b) 5.4 J/cm^2 From left to right: 400, 200, 100, 40 and 10 passes.

Figure 3.2: Optical micrographs of the exit side of the sample. In (b), dark lines are the laser cut region, while exit side damage is visible between the cuts, up to 50 microns from center of the cut. Electric field is parallel to cut direction and scan rate is 2000 μm/sec.

ESEM examination of the laser entrance surfaces revealed a high quality cut at the two lower fluences, but microcracking at the laser entrance side is occurring at the highest fluence as shown in Fig. 3.3. The 16 J/cm^2, 20 pass cut is all the way through the sample at some points while the cut is completely through for 100 passes. The cut depth is observed to be saturating as the number of passes increases for the two lower fluences. Fig. 3.4 shows the depth measured when using ESEM to observe the cut at the sample edge. The cut depth is seen to saturate at values

below the 75 μm thickness of the sample for 2.5 and 5.4 J/cm^2. A change in the profile of the machined groove occurs between 10 and 40 passes (10-30 μm deep) for the 5.4 J/cm^2 case shown in Fig. 3.5. The sidewalls of the channel becomes steeper and the appearance of exit side damage coincided with the steeper sidewalls. The appearance of rear side damage after a similar depth has been removed has been noted in other work and was suggested to be due to the collision of a surface Rayleigh wave and compression wave at the rear surface of the sample.[11] In that work, it was also observed that the ratio of the distance of the rear side damage from the center of the slot, w, divided by the sample thickness, d, was a constant for different glass thicknesses. The ratio w/d was found to be 0.75 in that work, similar to the ratio of w/d = 57/75 = 0.76 found here for the highest fluence.

(a) 2.5 J/cm^2 From left to right: 400, 200 and 40 passes.

(b) 5.4 J/cm^2 From left to right: 400, 200, 100, 40 and 10 passes.

(c) 16 J/cm^2 From left to right: 100 and 20 passes.
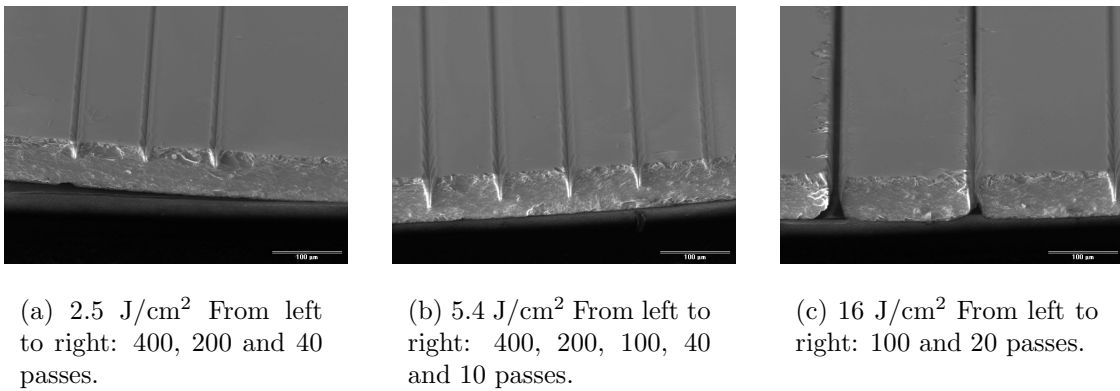
Figure 3.3: ESEM images of the edge of the quartz sample. Electric field is parallel to cut direction and scan rate is 2000 μm/sec. Scale bar in image is 100 μm.

Because the exit side damage was not noted until a certain depth of material was removed and the profile of the cut has become much steeper as depth increases as seen in Fig. 3.5(b), a refractive redirection of the beam by the edges of the cut was considered as a cause of the exit side damage. The geometry in Fig. 3.5(b) was considered using the linear refractive index of 1.54 for quartz at 800 nm, a half angle
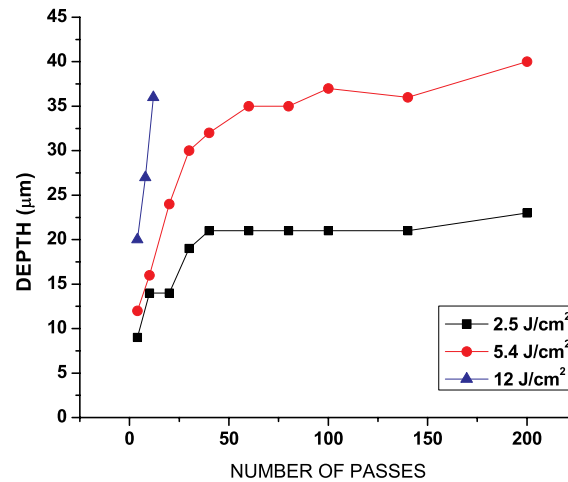
Figure 3.4: Cut depth as a function of fluence and number of passes. Electric field is perpendicular to the cut and scan rate is 2000 μm/sec.
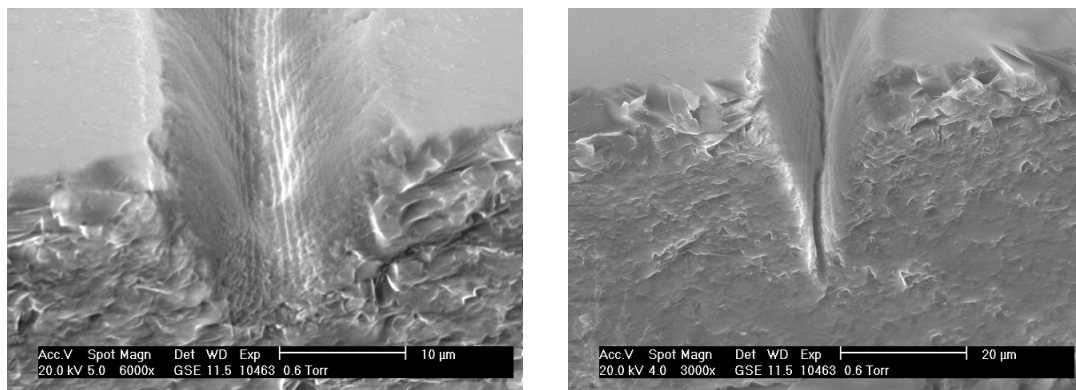
(a) 5.4 J/cm^2, 10 passes, no exit side damage noted.

(b) 5.4 J/cm^2, 40 passes, exit side damage occurs.

Figure 3.5: ESEM micrograph of the sample edge showing the increased steepness of the cut sidewalls as the number of passes increases.

of the cut of 13 degrees, and a cut depth of 31 microns. An exit position a distance 34 microns from the center of the slot to the closest exit side damage was calculated, compared with the measured value of 41 microns for 5.4 J/cm^2, 40 passes. The effect of the modification of the quartz index by the high laser intensities has been ignored in this calculation and a more detailed model including nonlinear propagation effects may give better agreement. It should be noted that this refractive mechanism would also be consistent with a constant w/d as sample thickness d changes.

A second consideration when assuming a refractive exit side damage mechanism is if enough transmitted power is available to damage the back side of the sample. Transmission measurements of 620 nm, 120 fs lasers focused on the surface of a fused silica sample found a decreasing transmission with increased fluence, starting at about 70 percent transmission at 2 J/cm^2 and decreasing to 40 percent as fluence increased to 16 J/cm^2.[14] Using these estimates for transmission and after accounting for the halving of laser fluence by the refraction, the transmitted fluence was estimated to be just above the measured 1 J/cm^2 damage threshold of the quartz for an incident fluence of 5.4 J/cm^2 and about three times the damage threshold for 16 J/cm^2 and was below the threshold for 2.5 J/cm^2, in agreement with experiment.

Dropping the fluence to 13 J/cm^2 eliminated the laser entrance microcracking problems and a scan in a square pattern 200 μm on a side was used to cut completely through the sample. In Fig. 3.6(a), note that extended exit side damage is absent near the corners of the pattern where the scan stops and changes direction. The lack of damage at the corner of the cut could also be explained by refraction and the changing sidewall geometry at that point. Along the slot, the beam is refracted into two spots, while at the corners the rounded corners would refract the beam into an arc. The reduced transmitted power density of the arc at the corner compared to the refraction of two beams in the groove could account for the lack of damage surrounding
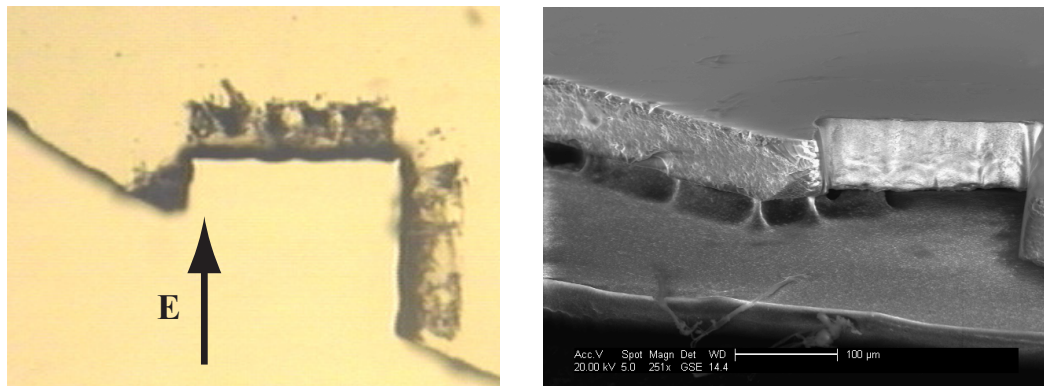
(a) Optical image of exit side of the cut. (b) ESEM image of the edge of the cut.

Figure 3.6: Optical and ESEM image of laser cut in quartz using 13 J/cm^2 and 200 passes around a square pattern at the edge of the sample. Electric field polarization is shown in (a). Scan speed is 2000 μm/sec.

the corner. Also, no dramatic difference in the amount of exit side damage is noted when changing the laser electric field orientation relative to the cut by changing scan directions. Fig. 3.6(b) shows an ESEM edge view of the sample. No entrance side microcracking was observed in this cut although cracking was observed on the cut sidewall near the exit.

Parameters were varied including number of passes, fluence, and focal position in order to better understand their effect on the exit side damage. Figs. 3.7(a) and 3.7(b) show the results of changes in fluence for a single scan and changes in the number of scans for a fixed fluence of 7.4 J/cm^2.

Fig. 3.7(a) shows an increase in the amount of exit side damage for increasing fluence while Fig. 3.7(b) shows that the amount of exit side damage surrounding the cut increases with the number of passes. In both Fig. 3.7(a) and 3.7(b) the exit side damage moves closer to the laser cut slot as the depth increases. The movement of the exit damage closer to the slot center is also consistent with a refractive exit side
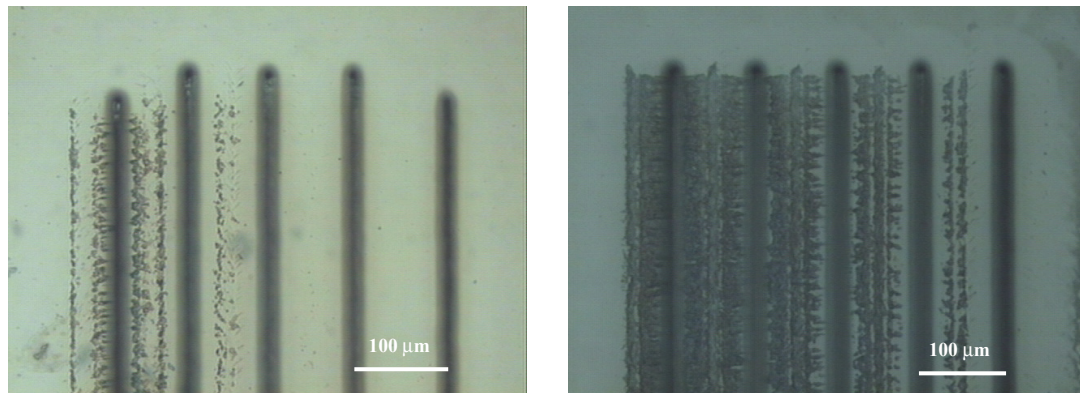
(a) Single passes made at different fluences. From right to left, fluences of 4.1, 5.4, 7.4, 9.7 and 12 J/cm^2.

(b) Fluence of 7.4 J/cm^2. From right to left; 1,2,3,4 and 5 passes.

Figure 3.7: Optical micrograph of the exit side of the sample for varying fluences and number of passes. Electric field is perpendicular to the cut and translation speed is 50 μm/sec.
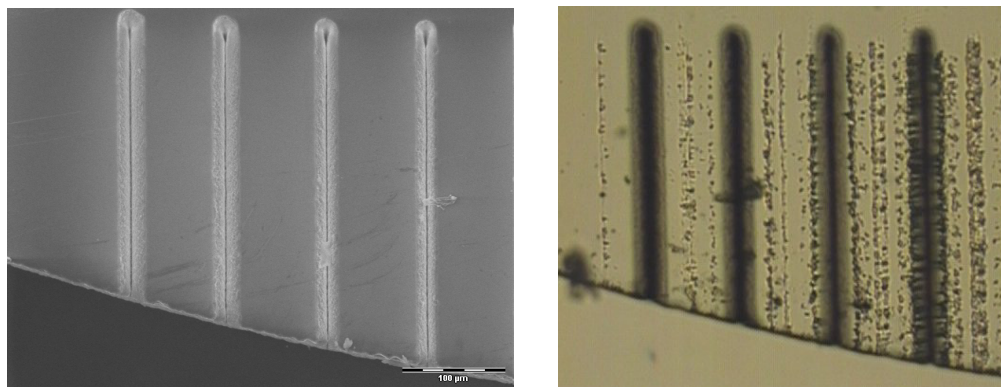
(a) ESEM image of laser entrance side for fluence of 9.7 J/cm^2 and different focal positions. From left: z = 14.6, 14.5, 14.4 and 14.3 mm.

(b) Optical image of same area with image focused on laser exit side.

Figure 3.8: ESEM and optical images of single pass cuts for different focal positions below the sample entrance location. A z position of 14.2 mm positions the sample surface at the beam focus and larger z values move the focus inside the sample. Electric field is perpendicular to the cut and scan speed is 5 μm/sec
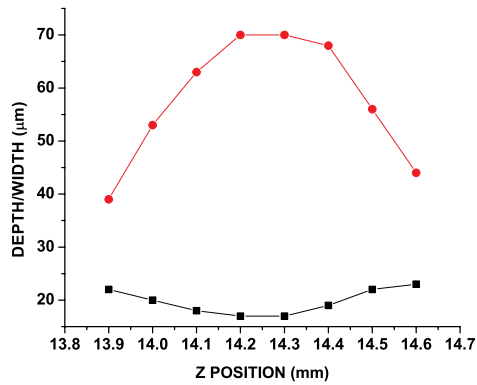
Figure 3.9: Entrance side cut width (squares) and depth (circles) of single pass cuts at 9.7 J/cm^2 as a function of the sample position. A z position of 14.2 mm positions the sample surface at the beam focus. Larger z values move the focus inside the sample.
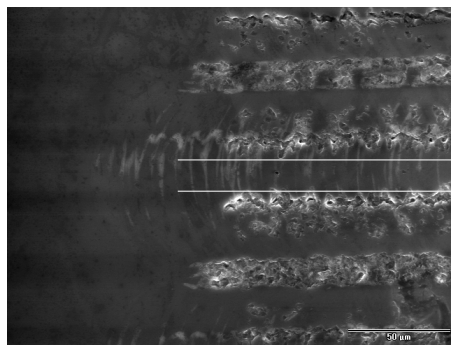
Figure 3.10: ESEM image of back side damage for single pass cuts at 9.7 J/cm^2. The two lines mark the edges of the entrance side of the cut at z = 14.3 mm as determined by comparison with optical images. Damage is observed at two locations on either side of the cut, $\sim$ 20 and 50 μm from the center of the cut.

damage mechanism. The influence of focal position and its effect on the exit side damage and entrance diameter is shown in Fig. 3.8 for the slowest scan rate available, 5 μm/sec. Fig. 3.8(a) shows the high quality of the entrance side while Fig. 3.8(b) shows that the exit side damage increases as the focal position becomes closer to the optimal position. The cut depth also increases and the entrance width of the cut decreases as the sample approaches the optimal focal position at z = 14.2 mm. The cut entrance widths and depths for different focal positions are plotted in Fig. 3.9.

Fig. 3.10 shows two damage regions on the exit side of the same sample. Damage about 50 μm from the center which is observed for shallower cuts and a damaged area 20 μm from the center of the cut which appears with deeper cuts. Again, the exit side damage moves closer to the position of the slot as the slot depth becomes larger.

3.4 Conclusions

Micromachined slots in AT cut quartz samples with no visible microcracking around the entrance side were obtained for fluences from 2.5–13 J/cm^2. At 16 J/cm^2, cracking surrounding the cut on the entrance side of the sample was seen. The laser exit side had damage within 50 μm of the center of the cut running parallel with the cut. This exit side damage ran parallel to the laser cut slot and moved closer to the slot as the depth of the slot increased.

3.5 Acknowledgements

REFERENCES

1. D. Du, X. Liu, and G. Mourou, "Reduction of multi-photon ionization in dielectrics due to collisions," *Appl. Phys. B*, vol. 63, pp. 617–621, 1996.

2. W. Kautek, J. Krüger, M. Lanzner, S. Sartania, C. Spielmann, and F. Krausz, "Laser ablation of dielectrics with pulse durations between 20 fs and 3 ps," *Appl. Phys. Lett.*, vol. 69, pp. 3146–3148, 1996.

3. M. Lenzner, J. Krüger, S. Sartania, Z. Cheng, C. Spielmann, G. Mourou, W. Kautek, and F. Krausz, "Femtosecond optical breakdown in dielectrics," *Phys. Rev. Lett.*, vol. 80, no. 18, pp. 4076–4079, 1998.

4. B. C. Stuart, M. D. Feit, S. Herman, A. M. Rubenchick, B. W. Shore, and M. D. Perry, "Optical ablation by high-power short-pulse lasers," *J. Opt. Soc. Am. B*, vol. 13, no. 2, pp. 459–468, 1996.

5. A. P. Joglekar, H. Liu, E. Meyerhöfer, G. Mourou, and A. Hunt, "Optics at critical intensity: Applications to nanomorphing," *PNAS*, vol. 101, pp. 5856–5861, 2004.

6. S. Ameer-Beg, W. Perrie, S. Rathbone, J. Wright, W. Weaver, and H. Champoux, "Femtosecond laser microstructuring of materials," *Appl. Surf. Sci.*, vol. 127–129, pp. 875–880, 1998.

7. H. Zheng, W. Zhou, H. Qian, T. Tan, and G. Lim, "Polarization-independence of femtosecond laser machining of fused silica," *Appl. Surf. Sci.*, vol. 236, pp. 114–119, 2004.

8. H. Varel, D. Ashkenasi, A. Rosenfeld, M. Wähmer, and E. E. B. Campbell, "Micromachining of quartz with ultrashort laser pulses," *Appl Phys. A*, vol. 65, pp. 367–373, 1997.

9. S. Nolte, M. Will, M. Augustin, P. Triebel, K. Zöllner, and A. Tünnermann in *Lithographic and Micromachining Techniques for Optical Component Fabrication*, vol. 4440 of *Proceedings of SPIE*, (Bellingham, WA), pp. 152–160, SPIE, 2001.

10. N. Kuriyama and Y. Ito, "Third international symposium on laser precision microfabrication," vol. 4830 of *Proceedings of SPIE*, (Bellingham, WA), pp. 567–572, SPIE, 2003.

11. E. Vanagas, J. Kawai, D. Tuzhilin, I. Kudryashov, A. Mizuyama, K. Nakumara, K. Kondo, S. Koshihara, M. Takesada, K. Matsuda, S. Joudkazis, V. Jarutis, S. Matsuo, and H. Misawa, "Glass cutting by femtosecond pulsed irradiation," *J. Microlith., Microfab., Microsyst.*, vol. 3, pp. 358–363, 2004.

12. D. J. Hwang, T. Y. Choi, and C. P. Grigoropoulos, "Liquid-assisted femtosecond laser drilling of straight and three-dimensional microchannels in glass," *Appl. Phys. A*, vol. 79, pp. 605–612, 2004.

13. J. M. Liu, "Simple technique for measurements of pulsed gaussian-beam spot sizes," *Opt. Lett.*, vol. 7, pp. 196–198, 1982.

14. D. von der Linde and H. Schüler, "Breakdown threshold and plasma formation in femtosecond laser-solid interaction," *J. Opt. Soc. Am. B*, vol. 13, no. 1, pp. 216–222, 1996.

Chapter 4

Conclusions and Recommendations

4.1 Conclusions

A large window of pulse energies exists where clean ablation of 20 nm Al films can be obtained with minimal damage to the substrate for pulses shorter than 4 ps. This pulse energy range was a factor of 2.6-7.3 times the clean ablation threshold for pulses less than 4 ps and decreased with increasing laser pulse width to ≤ 1.2 for 6 ns pulses.

When using the technique of varying laser energy with a gaussian spatial distribution to create ablation craters smaller than the laser spot size, there is a minimum ablation crater diameter, below which film deformation and frozen melt ejection appear. The minimum crater diameter obtained with complete ablation of the film was 130–260 nm for a 400 nm center wavelength, 400 fs pulse focused with an NA=0.85 objective. In the fluence range just above the damage threshold, nanobumps are formed whose height increases with pulse energy. As pulse energy increased further, nanojets began to appear in the center of the bump and grew up to 140 nm in height.

The sub-ps laser damage threshold of 20 nm Al films was measured to be two to three times higher than a theoretical model which assumes an equilibrium melting temperature and bulk specific heat.

Micromachined slots in AT cut quartz samples with no visible microcracking around the entrance side were obtained for fluences from 2.5–13 J/cm^2. At 16 J/cm^2, cracking surrounding the cut on the entrance side of the sample was seen. The laser

exit side had damage within 50 μm of the center of the cut running parallel with the cut. The damage moved closer to the slot as the depth of the slot increased. Two separate exit side damage regions were noted at distances of 20 and 50 μm from the center of the cut for cuts that were almost through the sample.

4.2 Recommendations for Future Work

For future work with quartz micromachining, frequency doubling the laser to 400 nm may help to enhance absorption compared to the 800 nm fundamental wavelength. Absorption of up to 90 % was noted in 400 nm ablation of quartz.[1] Further experiments would be useful to determine the mechanism of the exit side damage. For future work on nanobumps/nanojets, an investigation of the effect of film thickness on the nanojet height for Al and other ductile films would be of interest. An optimal film thickness which produced the longest length of the nanojet was found for gold films.[2]

REFERENCES

1. D. F. Price, R. M. More, R. S. Walling, G. Guethlein, R. L. Shepard, R. E. Stuart, and W. E. White, "Absorption of ultrashort laser pulses by solid targets heated rapidly to temperatures 1-1000 ev," *Phys. Rev. Lett.*, vol. 75, pp. 252–255, 1995.

2. J. Koch, F. Korte, T. Bauer, C. Fallnich, A. Ostendorf, and B. N. Chickov, "Nanotexturing of gold films by femtosecond laser-induced melt dynamics," *Appl. Phys. A*, vol. 81, pp. 325–328, 2005.

Appendix A

Ultrafast Optics

This section gives an introduction to ultrafast optics (picosecond duration and less) which are unique in their large spectral bandwidth compared to longer pulses. Pulse stretching of ultrashort pulses can occur when a pulse passes through a linear, isotropic material with dispersion or reflects from a mirror. During experimental work with ultrashort pulses distortion of the pulses (pulse lengthening) can occur. Equations to calculate this effect given the mirror or transmissive materials dispersion properties are provided. Distortions that occur at the focal plane when focusing pulses using a lens is discussed. The bandwidth and time-bandwidth product of a pulse with a Gaussian envelope is also derived. Finally, the use of an autocorrelator to determine pulsewidth is also discussed.

A.1 Pulse Bandwidth and Time-Bandwidth Product

The electric field, $e(t)$, of the laser pulse can be represented as:

$$e(t) = env(t) \cos\left(\omega_0 t - \beta z + \phi(t)\right) \tag{A.1}$$

where $env(t)$ is the real envelope of the cosine pulse with frequency $\omega_0 = 2\pi f_0$, $\beta(\omega) = \frac{\omega}{c}\sqrt{\varepsilon_r(\omega)} = \frac{\omega}{c}n(\omega)$, $\beta(\omega)$ is the propagation constant, $\varepsilon_r(\omega)$ is the relative dielectric permittivity of a medium at frequency ω , $n(\omega)$ is the index of refraction of the medium at frequency ω and $\phi(t)$ is the phase modulation.

The bandwidth of the pulse can be determined using Fourier transform methods. Since the spatial dependence in the z direction does not affect the bandwidth we will assume z = 0 in the following derivation. The other assumption used is that the pulse is "transform-limited". Transform-limited means that the pulse duration is completely determined by the spectral width. For this case the phase modulation, $\phi(t) = 0$. It can also be described as the shortest pulse obtainable given the available bandwidth.

The Fourier transform of $e(t)$ can be expressed as either:

$$E(f) = \int_{-\infty}^{\infty} e(t)e^{-i2\pi ft}dt \tag{A.2}$$

$$E(\omega) = \int_{-\infty}^{\infty} e(t)e^{-i\omega t}dt \tag{A.3}$$

and the corresponding inverse transforms are:

$$e(t) = \int_{-\infty}^{\infty} E(f)e^{i2\pi ft}df \tag{A.4}$$

$$e(t) = \frac{1}{2\pi} \int_{-\infty}^{\infty} E(\omega)e^{i\omega t}d\omega \tag{A.5}$$

A Gaussian envelope has the general form:

$$env(t) = e^{-\alpha^2 t^2} \tag{A.6}$$

The following Fourier transform pairs can be used to evaluate $E(f)$, given that e(t) has a Gaussian envelope.

$$e^{-\alpha^2 t^2} \Leftrightarrow \frac{\sqrt{\pi}}{\alpha}e^{-\left(\frac{\pi^2 f^2}{\alpha^2}\right)} \tag{A.7}$$

$$x(t)\cos(\omega_0 t + \phi) \Leftrightarrow 1/2 \left[X(f + f_0)e^{-j\phi} + X(f - f_0)e^{j\phi} \right] \tag{A.8}$$

Here $X(f)$ is the Fourier transform of x(t). From these equations, E(f) is found to be:

$$E(f) = \frac{\sqrt{\pi}}{2\alpha} \left[e^{\frac{\pi^2(f-f_0)^2}{\alpha^2}} + e^{\frac{\pi^2(f+f_0)^2}{\alpha^2}} \right] \tag{A.9}$$

The energy spectral density, $\psi(f)$, is:

$$\psi(f) = |E(f)|^2 \tag{A.10}$$

Solving for the half power points, f_{3dB} of $\psi(f)$ gives:

$$f_{3dB} = f_0 \pm \frac{\alpha\sqrt{2}\sqrt{\ln(2)}}{2\pi} \tag{A.11}$$

and FWHM of the spectral density, Δf, of:

$$\Delta f = \frac{\alpha\sqrt{2}\sqrt{\ln(2)}}{\pi} \tag{A.12}$$

A Gaussian envelope can be expressed as:

$$env(t) = e^{-\left(\frac{2\ln(2)t^2}{\tau_0^2} \right)} \tag{A.13}$$

where τ_0 is the Full Width Half Maximum (FWHM) of the pulse intensity, $I(t) \propto \langle e(t)^2 \rangle \propto env(t)^2$ and $\langle e(t)^2 \rangle$ is the time average of $e(t)^2$. Comparing Eq. A.13 and Eq. A.6 we see that:

$$\alpha = \frac{\sqrt{2}\sqrt{\ln(2)}}{\tau_0} \tag{A.14}$$

Substituting Eq. A.14 into Eq. A.12 gives:

$$\Delta f = \frac{2\ln(2)}{\pi\tau_0} \tag{A.15}$$

The time-bandwidth product, $c_b = \Delta t \Delta f = \tau_0 \Delta f$, (FWHM) for an unchirped Gaussian pulse is thus:

$$\Delta f \Delta t = \frac{2\ln(2)}{\pi} = .441 \tag{A.16}$$

Typically, experimental measurements of the spectral width are measured in terms of wavelength. A conversion factor between $\Delta\lambda$, the FWHM spectral width in terms of wavelength, and Δf is:

$$\Delta f = \frac{c\Delta\lambda}{\lambda_{1_{3dB}}\lambda_{2_{3dB}}} \simeq \frac{c\Delta\lambda}{\lambda_0^2} \tag{A.17}$$

and $\lambda_{1_{3dB}}, \lambda_{2_{3dB}}$, and λ_0 are respectively, the 3 dB wavelengths and the center wavelength of the measured spectrum. The shortest pulse which can be obtained with a given spectral bandwidth, Δf, is said to be bandwidth-limited (or alternatively transform-limited or uncertainty-limited). For a given envelope shape, the relationship $\Delta f \tau_0 \geq C_b$ holds where C_b is a constant dependent upon the pulse envelope. The shortest pulsewidth available given the bandwidth is: $\tau_0 = \frac{C_b}{\Delta f}$ and occurs for unchirped pulses, $\phi(t) = 0$. Time-bandwidth products for different pulse envelopes are given in Table A.1.[1]

Many papers in the literature use rms temporal and spectral widths rather than FWHM values. The rms pulse duration is defined as:[2]

$$\tau_{rms} = \left[\bar{t^2} - (\bar{t})^2\right]^{1/2} \tag{A.18}$$

where

$$\bar{t^n} = W_0^{-1} \int_{-\infty}^{\infty} t^n env(t)^2 dt \tag{A.19}$$

and

$$W_0 = \int_{-\infty}^{\infty} env(t)^2 dt \tag{A.20}$$

The spectral width can similarly be described in the form:

$$\Delta\omega_{rms} = \left[\bar{\omega^2} - (\bar{\omega})^2 \right]^{1/2} \tag{A.21}$$

where

$$\bar{\omega^n} = W_0^{-1} \int_{-\infty}^{\infty} \omega^n s_0(\omega) d\omega \tag{A.22}$$

and

$$s_0(\omega) = (2\pi)^{-1} \left| \int_{-\infty}^{\infty} env(t) e^{i\omega t} dt \right|^2 \tag{A.23}$$

Using these equations, the rms time-bandwidth product for a Gaussian envelope is determined to be $\tau_{rms}\Delta\omega_{rms} = 0.5$.

A.2 Pulse Stretching by Dispersion and Amplitude Filtering

The transmission of an initially unchirped pulse through a material or the reflection of a pulse from a mirror can stretch the pulse length from its initial value. For the case of transmission through a medium, a simple explanation for this phenomenon considers the different velocities of propagation, $v(\lambda)$, for the different wavelength components making up the pulse. Since the velocity of propagation, $v(\lambda) = \frac{c}{n(\lambda)}$ where $n(\lambda)$ in the index of refraction, varies with wavelength, the pulse becomes chirped, i.e.,

shorter and longer wavelengths become seperated within the pulse envelope and the pulsewidth becomes significantly longer if the path is long enough, (fiber optics as an example); or the bandwidth is great enough to cause a significant delay between the shorter and longer wavelengths due to the dispersion of the material, (femtosecond pulses).

The reflection or transmission of a pulse can be best investigated by working in the frequency domain. Using a Fourier transform, the incident pulse can be described as:

$$e(t) = \frac{1}{2\pi} \int\limits_{-\infty}^{\infty} E(\omega)e^{i\omega t}d\omega \tag{A.24}$$

Consider the reflection of a pulse from a mirror. The reflectivity of the mirror, r(ω) can be described by:

$$r(\omega) = A(\omega)e^{-i\phi(\omega)} \tag{A.25}$$

The reflected pulse, $e'(t)$ is found using the inverse Fourier transform:

$$e'(t) = \frac{1}{2\pi} \int\limits_{-\infty}^{\infty} E(\omega)A(\omega)e^{-i\phi(\omega)}e^{i\omega t}d\omega \tag{A.26}$$

A(ω) describes the effect on the amplitude of that spectral component and $\phi(\omega)$ is the phase shift. Lengthening of the reflected pulse can occur through two effects, amplitude filtering which occurs when the bandwidth of A(ω) is less than the bandwidth of the incoming laser pulse, and dispersion caused by the $\phi(\omega)$ term.

The phase shift, $\phi(\omega)$, can be expanded in a Taylor series about ω_0 to get:

$$\phi(\omega) = \phi(\omega_0) + \phi'(\omega_0)(\omega - \omega_0) + \phi''(\omega_0)\frac{(\omega - \omega_0)^2}{2!} + \phi'''(\omega_0)\frac{(\omega - \omega_0)^3}{3!} + ... \tag{A.27}$$

These derivatives are, respectively, the group delay $\phi'(\omega_0)$, the group velocity dispersion (GVD), $\phi''(\omega_0)$, and the "cubic term" $\phi'''(\omega_0)$ evaluated at ω_0. For transmission through a continuous material like glass, $\phi''(\omega_0) = \beta''(\omega_0)z$ where $\beta''(\omega_0)$ is the GVD per cm of material $(fsec^2/cm)$ and z is the pathlength through the material in cm and $\phi'''(\omega_0) = \beta'''(\omega_0)z$ where $\beta'''(\omega_0)$ is the cubic term per cm of material $(fsec^3/cm)$. Now consider the effect of amplitude filtering on the reflected pulsewidth with $\phi(\omega)$ a constant and

$$A(\omega) = e^{\left[\frac{-(\omega-\omega_0)^2}{2\omega_f^2}\right]} \tag{A.28}$$

Solving for the reflected FWHM pulsewidth, τ_1, given the original FWHM pulsewidth, τ_0, gives:

$$\tau_1 = \tau_0\sqrt{1 + \frac{4\ln(2)}{\omega_f^2\tau_0^2}} \tag{A.29}$$

The term describing the pulse stretching can be rearranged to have the form:

$$\sqrt{1 + \frac{K}{\frac{\omega_f^2}{\Delta\omega^2}}} \tag{A.30}$$

where $K \simeq 1$ is a constant. For $\omega_f^2 >> \Delta\omega^2$ minimal distortion of the pulsewidth occurs.

Now consider the reflection of an unchirped Gaussian pulse from a mirror with dispersion (GVD). Now assume $A(\omega) = 1$ and

$$\phi(\omega) = \phi(\omega_0) + \phi'(\omega_0)(\omega - \omega_0) + \phi''(\omega_0)\frac{(\omega - \omega_0)^2}{2!} \tag{A.31}$$

The first term just adds a phase shift and the second term creates only a time delay with no distortion of the pulse. The GVD term causes pulse spreading and chirping. Note that higher order terms become more important as the pulse becomes shorter.

The new FWHM pulsewidth τ_1, is related to the the initial FWHM pulsewidth τ_0 by the relation:

$$\tau_1 = \tau_0 \left[1 + \left(\frac{4\ln(2)\phi''(\omega_0)}{\tau_0{}^2} \right)^2 \right]^{1/2} \tag{A.32}$$

The pulsewidth of an initially unchirped Gaussian pulse as it travels through a dispersive medium can be described with the following equation:[2]

$$\tau(z) = \tau_0 (1 + (z/Ld_2)^2)^{1/2} \tag{A.33}$$

Where τ_0 is the initial FWHM pulsewidth of the pulse, $\tau(z)$ is the FWHM pulsewidth at distance z in the medium and Ld_2 is the second order dispersion length defined by:

$$Ld_2 = \frac{\tau_0^2}{4\ln(2)\,|\beta''(\omega_0)|} \tag{A.34}$$

Third order dispersion which includes the cubic term is discussed elsewhere.[2-4] It was discovered that second order dispersion of a Gaussian pulse will still produce a pulse with a Gaussian envelope while the third order dispersion may distort the pulse by making it asymetric and producing ripple in the envelope. Also note that the spectrum of the transmitted or reflected pulse will be unchanged since $A(\omega)$ is assumed to be a constant for pure dispersive processes with no absorption or amplitude filtering.

A.3 Stretching of Pulsewidth at Focus of a Lens

Several mechanisms in addition to GVD can affect the pulsewidth of ultrashort pulses at the focus of a lens. The effect of spherical and chromatic aberrations[5] as well as a radius dependent delay called propagation time difference (PTD)[6] have been analyzed. The time dependence of the pulse at the focal point has been calculated

for the case of uniform illumination of a lens using Fourier transform methods.[7] The intensity at the focal plane, $I_f(t)$, is found to be:

$$I_f(t) \propto \left[erf\left(\sqrt{2\ln(2)}\frac{t+T_0}{\tau_0} \right) - erf\left(\sqrt{2\ln(2)}\frac{t}{\tau_0} \right) \right]^2 \qquad (A.35)$$

where erf(t) is the error function given by

$$erf(t) = \frac{2}{\sqrt{\pi}} \int_0^t \exp(-\mu^2)d\mu \qquad (A.36)$$

$I_f(t)$ is seen to resemble a square pulse of duration T_0 with rise and fall times of approximately τ_0, the input pulse duration. T_0 is the PTD expressed as

$$T_0 = \frac{-a_0^2 \lambda_0}{2cf_0(n_0-1)} \left. \frac{dn}{d\lambda} \right|_{\lambda_0} \qquad (A.37)$$

where a_0 is the radius of the lens aperture, f_0 is the focal length of the lens at the center wavelength, λ_0, n_0 is the index of refraction of the lens at λ_0 and $\left. \frac{dn}{d\lambda} \right|_{\lambda_0}$ is the derivative of the index of refraction evaluated at λ_0. The temporal envelope is assumed to be Gaussian of the form in Eq. A.13

Focusing pulses which have a Gaussian spatial profile has also been considered.[8] Numerical methods rather than analytical solutions were developed for this case however. The effect of PTD is reduced for Gaussian pulses due to the reduced amplitude of the pulse at the lens outer radius[5] The effect of PTD is found to be dominant over GVD for pulses of 100 fs duration and longer in the visible and NIR.[9] The spatial FWHM was also calculated to be smaller than the CW case for pulses less than 50 fs in duration indicating that "breaking the diffraction limit" may be possible with ultrashort pulses.

A.4 Measurement of Pulsewidth Using an Autocorrelator

Pulsewidths of sub-picosecond pulses cannot be measured directly with a photodetector due to the relatively slow response time of the detectors, a few picosconds risetime for the fastest detectors available. The most widely used method to measure pulsewidth uses second harmonic generation (SHG) and time delay between the pulses to create a spatial autocorrelation trace.[10–12] The question then becomes how the width of the measured autocorrelation trace is related to the width of the actual pulsewidth. Different autocorrelation traces can be obtained depending upon whether or not a "backgound" signal appears as well as the averaging times of the signal. The autocorrelation trace can be in either "with background" or "background free" depending upon the alignment of the beams coming through the SHG crystal in the autocorrelator. The "with backgound" alignment has the two beams coming through the SHG crystal collinearly. The "background free" mode has the beams parallel but not collinear as they enter the focusing lens and cross each other with an intersection of the beams in the SHG material. The averaging times will determine whether phase information about the pulse is lost or not. The "fast" or "interferometric" autocorrelation retains phase information while the "intensity" or "slow" autocorrelation does not. The most common and easiest trace to produce experimentally is the "intensity" autocorrelation trace which is discussed here.

The slow autocorrelation with background can be expressed as:[12]

$$g_B^2(\tau) = 1 + 2\frac{\int\limits_{-\infty}^{\infty} env^2(t)env^2(t+\tau)dt}{\int\limits_{-\infty}^{\infty} env^4(t)dt} \tag{A.38}$$

The slow autocorrelation without background can be expressed as:

$$g_0^2(\tau) = \frac{\int\limits_{-\infty}^{\infty} env^2(t)env^2(t+\tau)dt}{\int\limits_{-\infty}^{\infty} env^4(t)dt} \tag{A.39}$$

Now solve for the FWHM of the autocorrelation trace assuming a Gaussian envelope. The integral in the denominator is a constant so the problem reduces to solving for the integral in the numerator. The following definitions are useful in solving for the autocorrelation function $g_0^2(\tau)$.

The time-autocorrelation function of a function g(t) is:

$$\psi_g(\tau) = \int\limits_{-\infty}^{\infty} g(t)g(t+\tau)dt \tag{A.40}$$

The Fourier transform of $\psi_g(\tau)$ is:

$$\psi_g(\tau) \Leftrightarrow G(f)G(-f) \tag{A.41}$$

where $G(f)$ is the Fourier transform of $g(t)$. Solving for the Fourier transform of $g_0^2(\tau)$, $G_0^2(f)$ and assuming a Gaussian envelope, $env(t) = e^{-\alpha^2 t^2}$, and using Eq. A.7 gives:

$$env^2(f) \propto e^{\frac{-\pi^2 f^2}{2\alpha^2}} \tag{A.42}$$

$$G_0^2(f) \propto e^{-\left(\frac{\pi^2 f^2}{\alpha^2}\right)} \tag{A.43}$$

Again using Eq. A.7 to perform the inverse Fourier transform gives:

$$g_0^2(\tau) \propto e^{-\alpha^2 \tau^2} \tag{A.44}$$

The FWHM of $g_0^2(\tau)$, $\Delta\tau$, is found to be:

$$\Delta\tau = \frac{2\sqrt{\ln 2}}{\alpha} \tag{A.45}$$

The property that an even real time function produces a pure real even transform was also used. Substituting Eq. A.14 into Eq. A.45 gives:

$$\Delta\tau = \sqrt{2}\tau_0 \tag{A.46}$$

So for a Gaussian pulse, the ratio of intensity to autocorrelation pulsewidth is:

$$\frac{\Delta\tau}{\tau_0} = \sqrt{2} \tag{A.47}$$

Autocorrelation/intensity pulsewidth ratios for different pulse envelopes are summarized in Table A.1.[1] Other methods such as FROG (frequency-resolved optical gating)[13,14] have been developed which can provide phase information (chirp information) about the pulse.

It should also be noted that the background-free autocorrelation method has a limitation due to errors induced by the nonparallel orientation of the wavefronts coming through the nonlinear crystal.[15] The limitation on pulsewidths which can be measured can be expressed as:

$$\tau > (a/c)sin(\gamma) \tag{A.48}$$

where a is the dimension of the spot at the crystal surface in which the beams overlap, c is the speed of light in a vacuum, and γ is the angle between the two incoming beams.

Table A.1: Transform-limited time-bandwidth products and autocorrelation/intensity pulsewidth ratios, $\frac{\Delta\tau}{\tau_0}$, (FWHM) for different pulse envelopes.

Intensity	$\frac{\Delta\tau}{\tau_0}$	$\Delta t \Delta f$
$1(0 \leq t \leq \tau_0)$	1	0.886
$\exp\left(-\frac{4\ln(2)t^2}{\tau_0^2}\right)$	$\sqrt{2}$	0.441
$sech^2\left(\frac{1.76t}{\tau_0}\right)$	1.55	0.315
$\exp\left(-\frac{\ln(2)t}{\tau_0}\right)(t \geq 0)$	2	0.11

REFERENCES

1. C. V. Shank and E. P. Ippen, *Dye Lasers*, ch. 4, p. 142. Berlin: Springer-Verlag, 1990.

2. S. A. Akhmanov, V. A. Vysloukh, and A. S. Chirkin, *Optics of Femtosecond Laser Pulses*, ch. 1. New York: American Institute of Physics, 1992.

3. D. Marcuse, "Pulse distortion in single-mode fibers," *Applied Optics*, vol. 19, no. 10, pp. 1653–1660, 1980.

4. D. Marcuse, "Pulse distortion in single-mode fibers. 3: Chirped pulses," *Applied Optics*, vol. 20, no. 20, pp. 3573–3579, 1981.

5. M. Kempe and W. Rudolph, "Impact of chromatic and spherical aberration on the focusing of ultrashort light pulses by lenses," *Optics Letters*, vol. 18, no. 2, pp. 137–139, 1993.

6. Z. Bor, "Distortion of femtosecond laser pulses in lenses," *Optics Letters*, vol. 14, no. 2, pp. 119–121, 1989.

7. Z. L. Horváth and Z. Bor, "Behaviour of femtosecond pulses on the optical axis of a lens. analytical description," *Optics Communications*, vol. 108, pp. 333–342, 1994.

8. Z. L. Horváth and Z. Bor, "Focusing of femtosecond pulses having gaussian spatial distribution," *Optics Communications*, vol. 100, pp. 6–12, 1993.

9. M. Kempe, U. Stamm, B. Wilhelmi, and W. Rudolph, "Spatial and temporal transformation of femtosecond laser pulses by lenses and lens systems," *J. Opt. Soc. Am. B*, vol. 9, no. 7, pp. 1158–1164, 1992.

10. A. Yariv, *Optical Electronics*, ch. 6, pp. 173–177. New York: CBS College Publishing, 1985.

11. J.-C. M. Diels, J. J. Fontaine, I. C. McMicheael, and F. Simoni, "Control and measurement of ultrashort pulse shapes (in amplitude and phase) with femtosecond accuracy," *Appl. Opt.*, vol. 24, no. 9, pp. 1270–1282, 1985.

12. K. L. Sala, G. A. Kenney-Wallace, and G. E. Hall, "Cw autocorrelation measurements of picosecond laser pulses," *IEEE J. Quantum Electron.*, vol. 16, no. 9, pp. 990–996, 1980.

13. K. W. DeLong, D. N. Fittinghoff, and R. Trebino, "Practical issues in ultrashort-laser-pulse measurement using frequency-resolved optical gating," *IEEE J.Quantum. Electron.*, vol. 32, no. 7, pp. 1253–1264, 1996.

14. G. J. Dixon, "Advanced techniques measure ultrashort pulses," *Laser Focus World*, vol. 33, no. 9, pp. 99–105, 1997.

15. S. A. Akhmanov, V. A. Vysloukh, and A. S. Chirkin, *Optics of Femtosecond Laser Pulses*, ch. 6. New York: American Institute of Physics, 1992.

Appendix B

Determination of Damage Threshold for Elliptical Beams

Liu has described an *in situ* technique to measure pulsed circular Gaussian spatial profile beam spot size and damage threshold.[1] The technique measures the damage diameters on the sample surface as pulse energy is varied and fits the data to a function to determine the the laser spot size and damage or modification threshold of the material. This section discusses the extension of this technique to an elliptical Gaussian beam.

The local fluence, $F(x, y)$, of an elliptical gaussian laser beam can be represented as:

$$F(x, y) = F_0 \exp\left[-2\left(\frac{x^2}{r_{0x}^2} + \frac{y^2}{r_{0y}^2}\right)\right] \tag{B.1}$$

where r_{0x} and r_{0y} are the radii where the fluence has dropped to $1/e^2$ of the maximum value and $F_0 = \frac{2E}{\pi r_{0x} r_{0y}}$ is the peak fluence obtained by an integration of the fluence over area to give the total energy, E, in the pulse. The total energy can be calculated as:

$$E = \int_{-\infty}^{\infty} \int_{-\infty}^{\infty} F(x, y) dx dy \tag{B.2}$$

This result can be used to determine F_0 as given above. For a circular gaussian beam with $r_{0x} = r_{0y} = r_0$; $F_0 = \frac{2E}{\pi r_0^2}$

The peak fluence is the relevant parameter in laser damage threshold measurements and the variation of the damage diameter vs. pulse energy can provide an estimate of the laser spot size and the peak damage fluence. The following describes the equations which can be used to determine the $1/e^2$ radii of the elliptical laser spot and threshold fluence (fluence at which melting or ablation occurs). This method is most accurate when the following conditions are met: single pulses are used, preventing growth of the diameter with successive pulses and the diffusion of deposited energy radially away from the area where it is absorbed is negligible, ensuring that the damage area is representative of the laser beam profiled. A large beam diameter relative to the diffusion length, $L_d = \sqrt{(D\tau_L)}$, where D is the thermal diffusivity of the material and τ_L is the laser pulse width, will ensure that mainly one-dimensional heat transfer into the material will occur for a bulk material and radial diffusion is not important. For pulses shorter than a critical pulse width, true thermal diffusion does not occur and the influence of hot electron diffusion becomes dominant.[2]

For a circular gaussian beam the fluence can be described as:

$$F(r) = F_0 \exp\left[-2\left(\frac{r^2}{r_0^2}\right)\right] \tag{B.3}$$

Assuming that a threshold fluence, F_{th}, exists, the damage diameter will extend to a radius, r_{th}, where the local fluence exceeds F_{th}. So the equation can be rewritten as

$$F_{th} = F_0 \exp\left[-2\left(\frac{r_{th}^2}{r_0^2}\right)\right] \tag{B.4}$$

and by rearranging becomes:

$$r_{th} = \frac{r_0}{\sqrt{2}}\sqrt{\ln\left(\frac{F_0}{F_{th}}\right)} \tag{B.5}$$

For elliptical beams, the same equation can be used for the damage radius along each axis, with the corresponding F_0 for elliptical beams.

Previous derivations in the literature appear to have used a nonstandard expression for the gaussian beam with an undefined parameter σ.[3] The threshold fluence was expressed as:

$$F_{th} = F \exp\left[-\left(\frac{r_{th}^2}{2\sigma^2}\right)\right] \tag{B.6}$$

Comparing Eqs. B.4 and B.6, the relationship $r_0 = 2\sigma$ is determined. This accounts for the factor of two difference between the resulting damage radius as a function of fluence that is derived from Eq. B.6 compared to Eq. B.5. This form seems to have been used in other work.[4,5]

The ablation crater cross-section of a 20 nm aluminum film using 4 ps laser pulses at 400 nm wavelength is shown in Fig. B.1. Ablation diameter was acquired using AFM for the two axes of the elliptical ablation crater. The inner and outer diameters, d_{in} and d_{out} as shown in Fig. B.1 were measured for the two axes of the elliptical beam. The following two equations were fit simultaneously to the measured major and minor axis diameter data:

$$d_{xth}(E) = \frac{d_{0x}}{\sqrt{2}} \sqrt{\ln\left(\frac{8E}{\pi d_{0x} d_{0y} F_{th}}\right)} \tag{B.7}$$

$$d_{yth}(E) = \frac{d_{0y}}{\sqrt{2}} \sqrt{\ln\left(\frac{8E}{\pi d_{0x} d_{0y} F_{th}}\right)} \tag{B.8}$$

where d_{xth} and d_{yth} are the measured diameters for the two axes of the beam and d_{0x}, d_{0y} and F_{th} are fit for both the inner and outer diameters, where d_{0x} and d_{0y} are the $1/e^2$ beam diameters. The fit to the data is shown in Fig. B.2

Plotting the data in a semi-log form as the damage radius squared vs fluence gives a clear visual representation of the damage threshold as shown in Fig. 2.18.
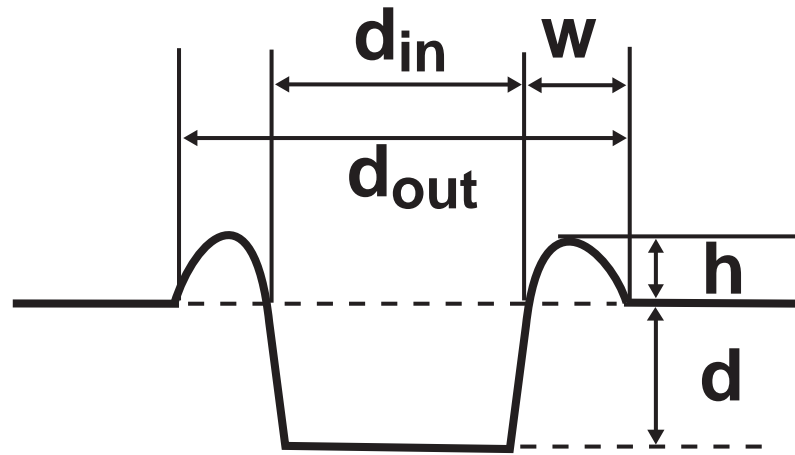
Figure B.1: Typical ablation crater illustrating the parameters used to characterize damage areas.
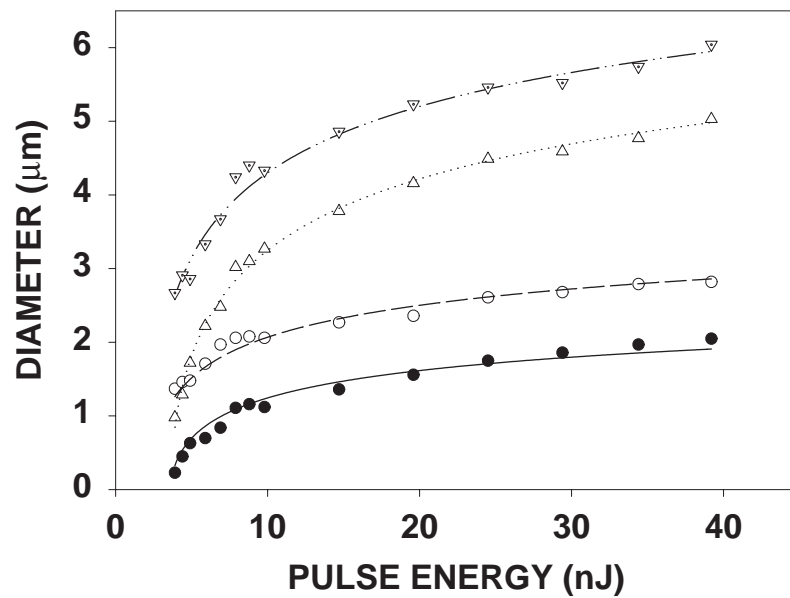

Figure B.2: Aluminum film ablation diameter as a function of laser pulse energy. Fits for both minimum and maximum axes. ∇, maximum d_{out}; $\triangle$, minimum d_{out}; $\circ$, maximum d_{in}; $\bullet$, minimum d_{in}.

REFERENCES

1. J. M. Liu, "Simple technique for measurements of pulsed gaussian-beam spot sizes," *Opt. Lett.*, vol. 7, pp. 196–198, 1982.

2. N. K. Sherman, F. Brunel, P. B. Corkum, and F. A. Hegman, "Transient response of metals to ultrashort pulse excitation," *Opt. Eng.*, vol. 28, pp. 1114–1121, 1989.

3. C. A. MacDonald, A. M. Malvezzi, and F. Spaepen, "Picosecond transient reflectance measurements of crystallization in pure metals," in *Beam-Solid Interactions and Phase Transformations* (H. Kurz, G. L. Olson, and J. M. Poate, eds.), vol. 51 of *Materials Research Society Symposium Proceedings*, (Warrendale, PA), pp. 277–282, Materials Research Society, 1986.

4. K. Furusawa, K. Takahashi, and S.-H.Cho, "Femtosecond laser micromachining of TiO$_2$ crystal surface for robust optical catalyst," *J. Appl. Phys.*, vol. 87, pp. 1604–1609, 2000.

5. J. Jandelheit, A. Horn, E. W. Kreutz, and R. Propawe, "Micromachining of metals and ceramics by nano- and piocosecond laser radiation," in *Proc. SPIE*, vol. 3223, pp. 32–42, 1997.